Politecnico di Torino

Department of Environment, Land, and Infrastructure Engineering

Master's degree in Petroleum and Mining Engineering

A.A. 2022/2023

Graduation session: November 2023

Data-driven modeling of an Aquifer Thermal Energy Storage (ATES) using machine-learning

Advisors:

Prof. Alessandro Casasso (POLITO)

Dr. Martin Bloemendal (TU Delft)

Dr. Riccardo Taormina (TU Delft)

Candidate:

Amirreza Parya

(ID 289093)

ACKNOWLEDGEMENT

I would like to express my profound gratitude for the remarkable journey I embarked on over the past two years, a journey that brought me to Italy and the Netherlands to pursue advanced studies. This endeavor has afforded me the privilege of delving deeply into the fascinating realms of the energy sector and artificial intelligence, unveiling a world of knowledge and exploration.

I extend my heartfelt appreciation to Dr. Alessandro Casasso and Dr. Marin Bloemendal, whose unwavering passion and profound expertise in geothermal energy, specifically the ATES system, have been instrumental in enriching my understanding of this intricate subject. I would also like to extend my sincere gratitude to Dr. Riccardo Taormina for his invaluable guidance in the realm of deep learning applied to ATES systems. Your professional supervising and technical discussions have been both enlightening and enjoyable.

Furthermore, I wish to express my gratitude to my dear brother, Hamidreza, for sharing his invaluable insights into simulation and machine learning science. His critical thinking and contributions to data-driven modeling have been invaluable to my research.

Lastly, I am deeply thankful to my mam and dad in Iran for their unwavering love and support throughout all my life journey.

Amirreza Parya
Delft, September 2023

ABSTRACT

Utilizing geothermal energy helps combat climate change by reducing greenhouse gas emissions. Efficient energy storage, especially through aquifer thermal energy storage (ATES) systems, is crucial. Despite potential, global ATES adoption is limited, mainly storing low-temperature heat. Improving efficiency involves storing higher-temperature water for use in colder seasons.

This study investigates the potential of the long short-term memory (LSTM), the deep learning approach to forecast ATES well temperatures for the Koppert-Cress horticultural facility. LSTM is a sub-branch of the deep learning method and deep learning is also the sub-branch of machine learning technology which is one kind of artificial intelligence (AI) technology. It delves into optimal data resolution, input and target variables, and loss functions. The research presents two LSTM-based model architectures, harnessing historically measured data to generate an extended forecast horizon concurrently. Robustness and stability are assessed via cross-validation, with model performances meticulously compared against original data. Furthermore, the LSTM-based model's performance is benchmarked against available data from the ATES system.

The findings indicate that when employing ATES historical data as input, the LSTM model demonstrates consistent and robust performance across the forecast horizon, rendering it suitable for operational deployment. Notably, the system predominantly operates in heating mode (37% of the time), reflecting the region's climate demands for heat. Moreover, a strong correlation is observed between environmental conditions and warm-well temperatures.

The initial LSTM model serves as a foundational part of this study for model development and data familiarization, with the primary objective of predicting the warm-well and the cold-well temperatures. Subsequently, the second LSTM architecture is used to perform forecasting over a longer time horizon to minimize the loss function, i.e., a function of the disagreement between predicted and actual data.

The research outcomes reveal the reliability of both models, characterized by low evaluation metrics for the regression errors (MSE, RMSE, MAE) and high accuracy (R^2) values in predicting wells' temperatures. The singular LSTM model achieves the highest R^2 of 0.97, while the parallel model achieves an R^2 of 0.87. This study advances the operational understanding of temperature outcomes from ATES wells through the application of LSTM deep learning. Future research avenues may explore the integration of this ML model into control systems and assess the quantification of heat requirements for upcoming time horizons within buildings, facilitating proactive energy management strategies.

Table of Contents

List of Tables

List of figures

List of equations

List of Abbreviations

1. ANN: artificial neural network
2. ATES/GeoTES: aquifer/geological thermal energy storage.
3. ATES: aquifer thermal energy storage system
4. BTES: borehole thermal energy storage.
5. CHP: combined heat and power.
6. COP: coefficient of performance.
7. DL: deep learning.
8. GHG: greenhouse gas
9. HE: heat exchanger.
10. HP: heat pump.
11. HT-ATES: high-temperature ATES.
12. HVAC: heating, ventilation, and air conditioning
13. LSTM: long short-term memory
14. LT-ATES: low-temperature ATES.
15. MAE: mean absolute error (m^3/m^3)
16. ML: machine learning
17. MSE: mean squared error $(m^3/m^3)^2$
18. R^2 or R-squared: coefficient of determination (%)
19. RMSE: root mean squared error (m^3/m^3)
20. RNN: recurrent neural network.
21. RTES: reservoir thermal energy storage.
22. UTES: underground thermal energy storage system.

Introduction

Heating and cooling buildings account for about 25% of global energy consumption making them a significant source of greenhouse gas (GHG) emissions. This is especially true for regions with temperate climates, where heating and cooling needs vary with the seasons. To reduce emissions associated with heating and cooling, the implementation of the aquifer thermal energy storage (ATES) system, is an effective strategy. These systems accumulate cooling capacity during winter and heating capacity during summer, ultimately reducing emissions when operating an air conditioning system. (Beernink. S. et. al., 2022).

An underground thermal energy storage system (UTES) consists of several key components, including one or more heat sources, an HVAC "heating, ventilation, and air conditioning" system, a shallow geothermal system, and underground storage tanks where thermal energy is stored. As shown in Figure 1A, external heat sources and shallow geothermal systems contribute to heat supply to meet user demand during times of high heating demand. In contrast, during periods of low or negative heat demand (indicating a need for cooling), a shallow geothermal system will store excess heat underground, as shown in Figure 1B. There are two main types of geothermal systems suitable for UTES, each with its own application, strengths, weaknesses, and design considerations. Closed-loop UTES are often referred to as borehole thermal energy storage (BTES), while open-loop UTES are referred to as aquifer thermal energy storage (ATES). It should be noted that, to our knowledge, UTES systems are currently installed primarily serving individual buildings and regional heating/cooling networks. However, UTES technology has potential for other applications, such as aquaculture, heating of anaerobic digesters, and low-temperature processes in food production, among many others. It is important to point out that all shallow geothermal systems, whether used for heating or cooling, are capable of storing thermal energy underground. However, the term "UTES" generally refers to systems specifically designed to store heat from external sources, such as solar heat or waste heat. To distinguish them from UTES installations, other shallow geothermal systems are referred to as "conventional" systems (Casasso. A. et. al., 2021).

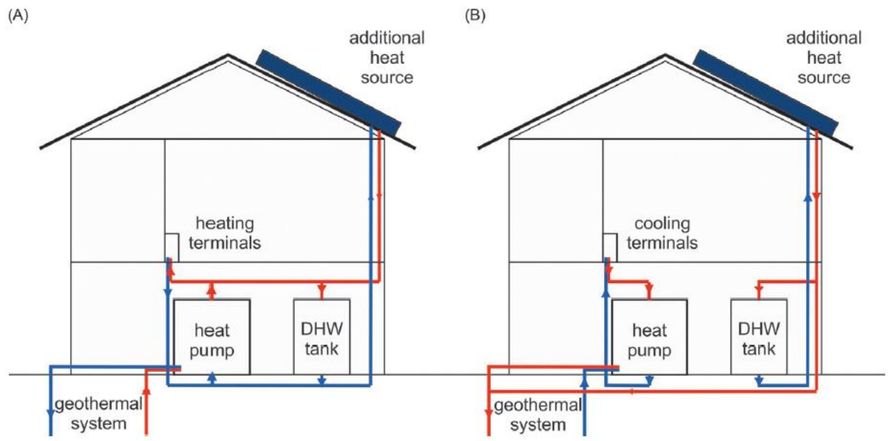

Figure 1: Link the main components of the UTES system operating in heating (A) and cooling (B) modes, namely: HVAC system (includes heat pump, domestic hot water (DHW tank, heating/cooling, and auxiliary terminals), backup heat generator and geothermal system. The red and blue lines represent heat transfer fluid flow is heated and cooled respectively (Ref: Casasso. A. et. al., 2022).

1.1 Distinguishing aquifer thermal energy storage (ATES) from conventional open-loop geothermal systems

Aquifer thermal energy storage (ATES) systems differ from conventional open-loop geothermal systems in the use of collection wells and injection wells. In traditional open-loop systems, each well serves a specific purpose. The production well is strategically located upstream in the direction of groundwater flow, while the injection well is located downstream. This arrangement facilitates the alternating injection of warm water (as shown in Figure 2A) and cold water streams (as shown in Figure 2B). In contrast, the ATES system is divided into two distinct regions: a warm zone and a cold zone. During the cooling season (as shown in Figure 2C), cold water is drawn, which then absorbs heat from the building and the additional heat source. This now-heated water is then pumped back into the aquifer as warm water. In contrast, during the heating season, hot water previously pumped is withdrawn, after releasing stored heat into the building (as shown in Figure 2D). It is then returned to the cold well as cold water. Compared with the conventional open-loop system, the ATES system shows improved efficiency. This efficiency increase, usually measured by the heat pump's coefficient of efficiency (COP), is the result of the ATES system extracting colder water for cooling and hotter water for heating, thus being optimal. optimize its performance in both operating modes (Casasso. A. et. al., 2022).

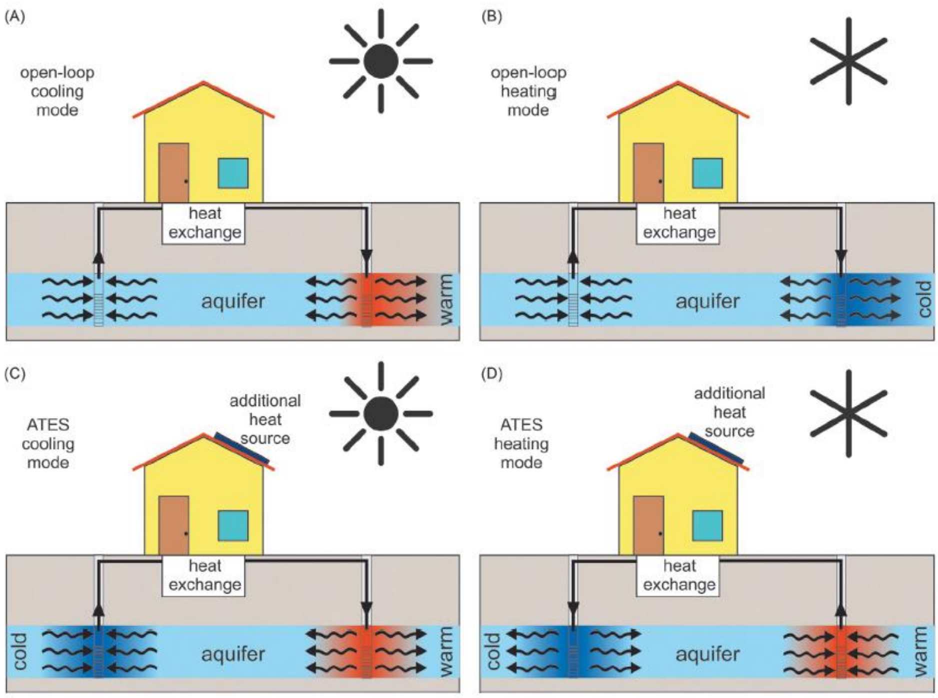

Figure 2: Open loop geothermal system (A: cooling mode; B: heating mode) and an aquifer thermal energy storage (ATES) system (C: cooling + heat injection; D: heating + cold injection) (Casasso. A. et. al., 2022).

1.2 Aquifer thermal energy storage (ATES) system

The reduction of greenhouse gas (GHG) emissions in urban environments has led to the widespread adoption of the aquifer thermal energy storage system (ATES), not only in the Netherlands but also around the world. ATES systems are characterized by reduced primary energy consumption and greenhouse gas emissions compared with conventional systems, but they still require energy inputs. significantly, including electricity to power heat pumps and circulating water pumps, as well as occasional dependence on fossil fuels for boilers to reach full heat capacity. therefore, improving the performance of the ATES system can further reduce greenhouse gas emissions and reduce pressure on the power grid. The initial investment for ATES systems is relatively high and depends on their maximum heating capacity. As a result, ATES systems are typically designed to meet basic heating needs, covering about 80% of total heat demand. Additional installations, often using peak (gas) boilers, are responsible for meeting peak heating demand. A cost-effective approach to increase heating capacity and reduce dependence on peak boilers is to increase the temperature difference between warm and cold wells. However, in many systems, water cooling is limited due to the risk of freezing in the heat pump evaporator during winter cold tank charging and potential condensation problems in the building during the winter. However, it can result in the availability of the process of direct cooling of the cold well in the summer. Therefore, increasing the temperature of the warm well appears as a promising strategy to improve heating capacity while enhancing the efficiency of the heat pump, or even making it redundant under extreme conditions. specifically. However, in most countries, regulatory restrictions limit warm well injection temperatures in the ATES system to either 25°C or 30°C, making it difficult to issue such system changes, even inaccessible. Fortunately, many regulatory agencies allow the application of high-temperature ATES (HT-ATES) as a pilot project.

In search of sustainable heating and cooling solutions, the ATES system was initially installed in a greenhouse by the horticulture company Koppert-Cress in 2012. Later, as part of a Ha Noi research project with a focus on reducing greenhouse gas emissions and the above aspects, this ATES system was converted into a pilot HT-ATES system in 2015. This study dives into designing and implementing an LSTM model for predicting the wells' temperature after converting the LT-ATES system to the HT-ATES one (Bloemendal. M. et. al., 2022).

1.3 Machine learning

1.3.1 Introduction to machine learning

Machine learning is similar to teaching computers to learn from examples (available data). Instead of telling them exactly what to do, lots of examples are shown to them, and they figure out patterns in their own decision. It helps computers make decisions and predictions without being explicitly programmed.

1.3.2 Introduction to deep learning

Deep learning is a method used in ML where computers learn to do tasks by looking at lots of examples. It's like teaching a computer to recognize patterns, such as images speech, or time series data, by showing it many different examples of those patterns. The computer uses complex algorithms inspired by the human brain neuron architecture to understand and interpret the data it's given. As it sees more examples, it gets better at recognizing these patterns and can make predictions or decisions based on what it has learned.

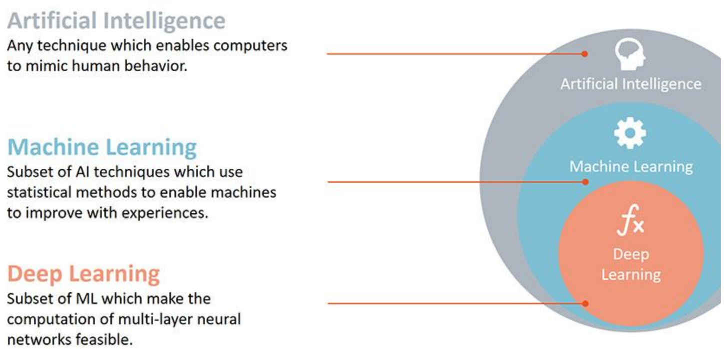

Figure 3: Artificial intelligence vs machine learning vs deep learning

1.3.3 Neuron layers

In deep learning, neurons are like the building blocks of the system, inspired by the way human brains work. They receive inputs, process them using mathematical operations, and produce an output. These neurons are organized into layers, forming a neural network, which helps the computer understand complex patterns in data.

1.3.4 Epochs

Epochs refer to the number of times the entire dataset is used to train the neural network. During each epoch, the computer goes through all the examples in the dataset, learns from them, and adjusts its internal settings to improve its accuracy in making predictions or recognizing patterns. Think of epochs as the computer's way of studying and revising from a textbook multiple times to better understand the material.

1.3.5 Batches

Batches, on the other hand, break down the dataset into smaller chunks. Instead of processing all the examples at once, which can be overwhelming for the computer's memory and processing power, the data is divided into batches. The neural network learns from each batch of data, makes adjustments, and then moves on to the next batch. Batches allow the computer to learn in manageable steps, similar to how you might learn a large topic by studying smaller sections at a time rather than trying to understand everything all at once.

1.3.6 Dense layer

The last block in the LSTM model, the dense layer, connects every neuron in the preceding layer to every neuron in the dense layer. Its great degree of neuronal connectivity accounts for its dubbed "dense" nature.

In an LSTM network, the recurrent layers—which resemble LSTM layers—activate often before the dense layer. The task of a thick layer is to transform the data from the prior layers into the final data. The neurons in the dense layer submit the input to an activation function and a weighted sum.

1.3.7 Machine Learning

Machine learning (ML) represents a subset of artificial intelligence that specializes in creating adaptive algorithms that can make decisions based on data, rather than conforming to static programming instructions. The main goal of ML is to empower computer programs to improve their performance on specific tasks through experiential learning. In the field of astronomy and geosciences, the potential benefits of applying ML are significant. Although the integration of ML techniques into these fields is happening gradually, there are still some published studies using ML methods in these fields (Bouchefry. K. et. al., 2020).

1.4 Deep learning - LSTM model

Deep learning (DL) techniques have attracted considerable attention due to their ability to efficiently capture the complexity of highly non-linear systems. In the field of nonlinear time series data modeling, recent studies have highlighted the potential of DL methods, especially LSTM (long short-term memory) networks. These DL approaches have shown significant improvements in prediction accuracy, scalability, and regional generalization capabilities compared with traditional conceptual models (Shamshirband et al., 2019). LSTM models, specifically designed for the analysis of sequential data such as time series, have shown great promise in a variety of applications. For example, Kratzert et al. (2019) successfully applied LSTM models in more than 500 basins in the United States, yielding improved flow predictions compared to conventional conceptual models. For a deeper understanding of the LSTM architecture, you can refer to Kratzert et al. (2018), while Figure 3 provides a visualization of a standard LSTM plot.

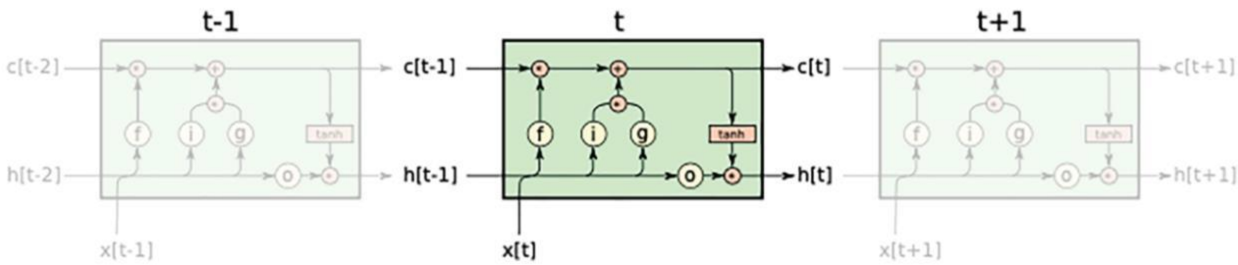

Figure 4: Standard LSTM model visualization. In the context of this description, the symbols are as follows: c[t] represents the state of the cell at time step t. h[t] is the hidden state at step t. x[t] represents the input at time step t. f represents the gate of oblivion. I correspond to the front door. g denotes a cell update. o represents the exit door. (Ref: towardsdatascience.com)

1.5 Problem statement

In the context of combating climate change and reducing greenhouse gas emissions, the integration of renewable energy sources and sustainable heating and cooling solutions has become increasingly vital. One innovative approach to address this challenge is the adoption of aquifer thermal energy storage (ATES) systems. Originally designed as low-temperature

ATES (LT-ATES), these systems have evolved into high-temperature ATES (HT-ATES), offering improved performance and expanded applicability. However, the transition of ATES systems from LT-ATES to HT-ATES presents both challenges and opportunities. This transformation involves significant alterations in the temperature dynamics of injected and extracted water in wells, crucial for harnessing thermal energy efficiently. The growing reliance on intermittent renewable energy sources underscores the need for effective energy storage solutions, encompassing electricity and heat. Within this context, the subsurface offers a promising avenue for storing substantial heat quantities, predominantly through ATES systems. Despite its potential, ATES technology remains relatively niche, with the Netherlands hosting 90% of these systems globally (Casasso. A. et. al.,2022). Most existing ATES systems primarily store low-temperature heat (below 30°C) (Casasso. A. et. al.,2022). To enhance energy density and overall efficiency, it becomes imperative to explore methods for efficiently storing higher-temperature water in aquifers during warm seasons and subsequently recovering this higher-exergy heat for heating in colder periods. To address these multifaceted challenges and unlock the full potential of HT-ATES systems, this research aims to employ machine learning (ML) models a subset of artificial intelligence to predict outcomes resulting from dynamic changes in input data, including water temperature, flow rates, and more. By leveraging ML techniques, this study seeks to overcome barriers associated with temperature management in ATES systems during the transition from LT-ATES to HT-ATES, ultimately contributing to the advancement of sustainable heating and cooling solutions within the broader context of renewable energy integration.

1.6 Objective

In this thesis, the following objectives will be pursued:

1- Develop a machine learning (ML) model, with a focus on deep learning techniques, tailored to the specific requirements of an aquifer thermal energy storage (ATES) system.
2- Identify and evaluate the most suitable ML approaches for accurately replicating the complex operational dynamics of an ATES.

1.7 Organizing of thesis

This report is organized into the following chapters:

1- **Introduction:** Chapter 1 introduces the aquifer thermal energy storage (ATES) system, deep learning, and long short-term memory (LSTM). It also outlines the problem statement and the study's objectives.
2- **Theoretical Background and Literature Review:** Chapter 2 provides an overview of the theoretical foundations relevant to the study and conducts an extensive review of the existing literature in the field.

3- **Methodology:** Chapter 3 delves into the methodology employed in the study. It covers the datasets used, and the data processing procedures, and provides an insight into the model architectures applied.
4- **Results:** Chapter 4 is dedicated to presenting the study's results, featuring data visualizations and a detailed analysis of the achieved outcomes.
5- **References**

Literature review

2.1 Basic of ATES

An ATES (aquifer thermal energy storage) system comprises a pair of wells, one cold and one warm, interconnected with a heat pump (HP) through a chilled water network and a heat exchanger. These wells serve as the source and sink for groundwater. Submersible pumps are employed to transfer groundwater between the two wells via the heat exchanger, facilitating heat exchange with the building cooling/heating system.

During the summer, when cooling is needed, the system utilizes cold groundwater directly for cooling purposes. Conversely, in the winter when heating is required, the heat pump's condenser provides heating at the desired temperature. Meanwhile, the heat from the evaporator side of the heat pump is extracted from the warm well, cooling down the groundwater and effectively storing cooling capacity in the cold well. The operation of the heat pump and submersible pumps necessitates electricity.

In the summer, the heat pump is mostly idle as free cooling can be directly obtained from the cold well. However, when the cooling capacity of the cold well falls short, the heat pump can be activated to provide additional cooling to the building. The cooling capacity generated at the evaporator is supplied to the building, while the heat produced at the condenser side is either stored in the warm well or dissipated to the outside air using a dry cooler.

In cases where there is a simultaneous demand for heating and cooling, both the heat produced at the condenser and the cooling capacity from the evaporator are delivered to the building. The proportion of heating to cooling demand determines whether the ATES system supplies extra heat to the heat pump or direct cooling to the building.

When the heating and cooling requirements of the building are imbalanced over multiple years, a dry cooler is employed to store excess heat during the summer or surplus cooling capacity in the winter. This stored energy can then be utilized to meet the energy demand in the subsequent season. Operating the dry cooler involves electricity usage for circulation pumps and ATES well pumps (Beernink. S. et. al., 2022).

2.2 LT-ATES transition to HT-ATES for enhancing energy efficiency

Aquifer thermal energy storage (ATES) systems, when combined with a heat pump, play a pivotal role in generating and storing both heat and cold, thereby reducing energy consumption for space heating and cooling in buildings. In many countries, these systems traditionally limit the temperature of stored heat to a maximum of 25-30°C. However, when higher-temperature heat sources are available (such as waste heat or solar heat), it becomes more efficient to store heat at elevated temperatures. This not only enhances the performance of the heat pump but can also make an abundance of heat resources possible. Consequently, there exists significant potential for achieving additional energy savings by transitioning from conventional low-temperature ATES systems to high-temperature ATES (HT-ATES).

This transformative approach has been successfully implemented and tested in the Netherlands, specifically for the Koppert-Cress greenhouse. The greenhouse has been utilizing a low-temperature ATES (LT-ATES) system since 2012. However, starting in 2015, there was a gradual increase in the storage temperature, with the warm well now capable of storing heat at temperatures of up to 40°C (Bloemendal. M. et. al., 2022)

2.3 Optimizing energy storage on ATES by adopting the machine-learning

The transition towards a net-zero carbon economy has spurred substantial growth in renewable energy production both in the United States and worldwide. However, among the various renewable energy resources, wind and solar power have emerged as the fastest-growing sectors. While they contribute significantly to the energy mix, they also introduce challenges due to the intermittent nature of electricity generation, exacerbating the supply-load imbalance on electric grids. For instance, in California, the electricity demand typically surges by approximately 13 GW from noon to nighttime on an average day. Unfortunately, this peak in demand coincides with a reduction in solar energy supply. To tackle this issue, the concept of reservoir thermal energy storage (RTES) has gained prominence. RTES involves injecting hot fluid into a subsurface reservoir and later recovering the geothermal energy when needed. This approach holds promise for rectifying supply and load imbalances on a grid-scale, thanks to its substantial storage capacity and dispatchable nature. It's worth noting that RTES goes by other names such as aquifer/geological thermal energy Storage (ATES/GeoTES), which employs a permeable formation to store thermal fluid, and borehole thermal energy storage (BTES), which uses closed pipelines to store thermal fluid, with heat transfer to the surrounding formation through thermal conduction (Jin, W. et. al., 2022).

The inception of RTES can be traced back to 1965 in Shanghai when multiple textile factories began storing cold water during the winter months for later use in cooling during the hot summer season (Shi. X. et. al., 2016).

The substantial computational requirements of physical modeling, coupled with the time-consuming pre and post-processing steps, often deter stakeholders from investing in reservoir thermal energy storage (RTES). They require rapid evaluations and may not have access to supercomputing resources (Jin. W. et. al., 2021).

As recognized by Bergen (Bergen. K.J. et. al., 2019) machine learning emerges as one of the most potent tools for tasks such as surrogate model development, geoscience exploration, and geoengineering. In the realm of subsurface energy engineering, the adoption of machine learning has experienced a remarkable surge in recent years.

2.4 LSTM model mechanism and its operation on time series data

Long short-term memory (LSTM) networks are a specialized type of recurrent neural network (RNN) designed to address the vanishing gradient problem and better capture long-range dependencies in sequential data. What sets LSTMs apart are their unique gating mechanisms, which endow them with the ability to perform selective operations on their cell state.

The key components of an LSTM are the forget gate, the input gate, and the output gate. These gates play pivotal roles in shaping the behavior of the LSTM network:

1. **Forget Gate**: The forget gate allows an LSTM to selectively forget or retain information stored in its cell state from previous time steps. It does this by learning to weigh the importance of each piece of information, making it an invaluable tool for preventing irrelevant or outdated data from impacting the current state.

2. **Input Gate**: The input gate facilitates the selective updating of the cell state with new information from the current time step. It controls which parts of the new input information are relevant and should be incorporated into the cell state, thereby ensuring that only pertinent data is integrated.

3. **Output Gate**: The output gate determines what information from the cell state should be revealed as the output of the current time step. This allows the LSTM to selectively output information that is most relevant to the task at hand, contributing to its adaptability and effectiveness in capturing long-term dependencies.

The combined operation of these gates empowers LSTMs to handle sequences with extended temporal dependencies effectively. Tasks that require modeling and prediction of sequences with intricate and long-lasting patterns, such as natural language processing, speech recognition, and time series forecasting, greatly benefit from the advanced capabilities of LSTMs. These networks have proven their worth in numerous applications where understanding and utilizing past information to make informed decisions about future events is critical.

Methodology

3.1 Study area

Koppert-Cress, a horticulture company located in the Western Netherlands region, implemented the ATES system in 2012, consisting of 4 hot wells and 4 cold wells, as shown in Figure 4. Koppert-Cress greenhouses exhibit a substantial heat need during the winter, as opposed to their cooling needs during the summer months. The excess heat is thus captured near their greenhouse and stored in hot water wells in the summer for use in the winter. This heat capture includes various 'passive' sources, such as solar panels, water heat, and waste heat from a nearby combined heat and power (CHP) facility.

Following the transition from low-temperature ATES (LT-ATES) to high-temperature ATES (HT-ATES) in 2015, these additional heat sources and some other cold sources were gradually incorporated into heating and cooling systems. The temperature of the heat obtained from these additional sources fluctuates throughout the year, of which part is available at temperatures above 25°C (Bloemendal et al., 2020).

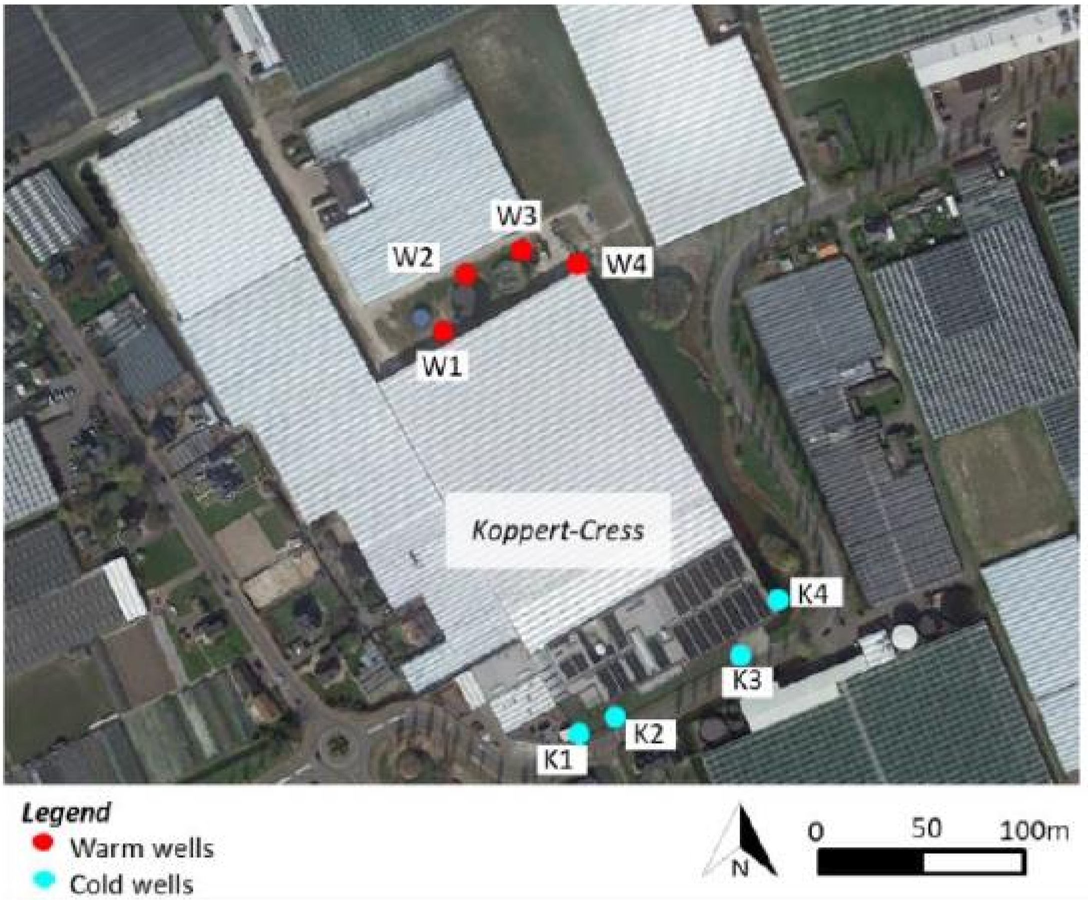

Figure 5: Koppert-Cress greenhouse site – well locations (Ref: Bloemendal et al., 2020).

The strategic integration of multiple heat sources into the ATES system has significantly improved the energy efficiency and sustainability of Koppert-Cress operations. The company has effectively harnessed a variety of heat sources, each contributing to the overall heating and cooling needs of its greenhouses.

Solar panels, a clean and renewable source of energy, have been harnessed to capture solar energy and convert it into heat during sunny times. In addition, the use of waste heat from a nearby combined heat and power plant (CHP) not only reduces energy waste but also promotes a circular economy by reusing excess heat that would otherwise be wasted.

The transition from LT-ATES to HT-ATES in 2015 marks a significant step forward in energy storage capabilities. High-temperature storage effectively retains heat at high temperatures, which is perfect for meeting the high heating needs of a greenhouse during colder months.

By combining these different heat sources and optimizing their use through the ATES system, Koppert-Cress has succeeded in creating a flexible and sustainable solution to meet heating and cooling needs. This approach not only reduces the company's carbon footprint but also serves as a model for sustainable practices in the horticulture industry.

3.2 Dataset

To evaluate the energy performance of the Koppert-Cress ATES system, various environmental and operational factors are continuously monitored. Specifically, operational data from the system's wells were collected between 2012 and 2023, providing information with a 5-minute resolution. This data includes important parameters such as cold and warm wells' temperatures, flow rate (both inlet and outlet), flow direction, and thermal energy for the eight wells in the system.

This comprehensive data set enables a detailed analysis of ATES system performance over time. With such detailed information, Koppert-Cress can closely monitor the operation and efficiency of wells, ensuring optimal system operation and meeting greenhouse heating and cooling requirements. By continuously monitoring these operational aspects, Koppert-Cress can make informed decisions to improve energy efficiency, reduce energy waste, and make the necessary adjustments to maintain energy efficiency. maintain sustainable and environmentally friendly gardening practices. This commitment to data-driven insights underscores their commitment to efficiency and environmental friendliness in their operations.

3.3 Metrological data

This study, in addition to utilizing the operational data collected from ATES system wells of the Koppert-Cress, also uses environmental data obtained from the Royal Netherlands Meteorological Institute (www.knmi.nl). This environmental data is an important input to machine learning models as driven data that detects and captures temperature changes in hot and cold wells.

By integrating this external environmental data into its ML model, improves its ability to understand and predict how natural factors, such as weather conditions and seasonal changes, affect the performance of its ATES system. This data-driven approach not only helps optimize energy management but also reinforces their commitment to sustainable practices by minimizing energy consumption and maximizing resource efficiency.

3.4 Selecting the proper machine learning model

In this thesis, when time series data is available for 5-minute intervals, the choice of deep learning technique is very important. In the field of deep learning, two main methods can be used for this purpose:

Recurrent neural networks (RNNs) and long short-term memory networks (LSTMs). Given the large length and volume of the data set, it is necessary to consider the “forgetting problem” associated with the RNN method.

The RNN model, although suitable for sequential data, has limitations when it comes to long-term dependence on the data. Information from earlier time steps tends to be forgotten or "deleted" as it travels over the network. This can lead to suboptimal performance when capturing complex patterns or relationships in the data (Figure 5).

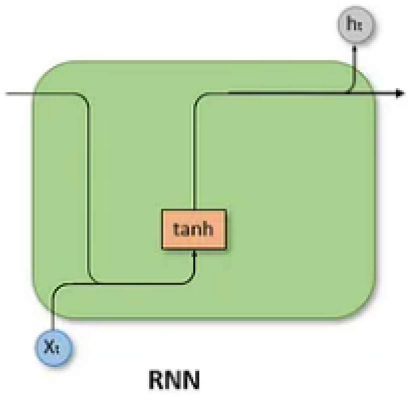

Figure 6: Recurrent neural networks (RNNs) (Ref: towardsdatascience.com)

To overcome this limitation, the decision to use the LSTM method was made. LSTM, which stands for long short-term memory, is an enhanced variant of the RNN model. What sets LSTM apart is its ability to selectively store and retain information in longer sequences through the use of internal neural connections. These connections, often referred to as gates, allow the LSTM model to remember and efficiently use relevant information from past time steps, thereby mitigating the forgetting problem associated with standard RNNs (figure 6).

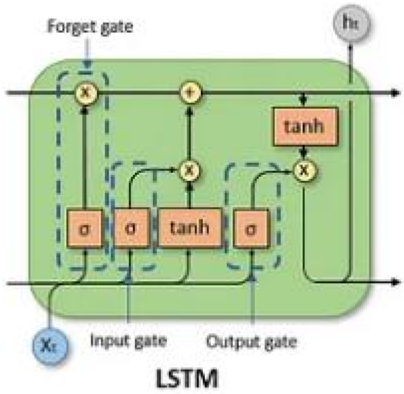

Figure 7: Long short-term memory (LSTM) (Ref: towardsdatascience.com)

By choosing an LSTM for our deep learning model, we take a proactive approach to ensure that the model can capture and maintain important patterns and dependencies in a variety of time series data. This decision reflects a deep understanding of the challenges posed by the dataset and demonstrates a commitment to using the most appropriate techniques to achieve accurate and insightful results in the thesis.

3.5 Different LSTM model architectures in this study

In this study, LSTM-based model architectures were chosen to predict warm and cold wells operating temperatures. Four separate architectures were designed and tested specifically for this study. Each of these architectures uses two groups of LSTMs, effectively integrating both the look-back window and forecast horizon data from the sequencer. These architectures are like singular LSTM topologies, cascade LSTM, or parallel LSTM configurations.

In the following, detailed descriptions of the four model architectures will be presented, providing a comprehensive understanding of their design and functionality.

3.5.1 Model 1

Model 1, as illustrated in Figure 7, features a single LSTM with one layer that is connected to a dense layer. The LSTM component is responsible for sequentially processing historical data from the past L days, often referred to as the "look-back window." It operates continuously up to the current time and generates the final output. All data from the geothermal wells and meteorological sources are utilized as input for this model. The outputs generated by the LSTM are combined and directed into the Dense layer, which concurrently produces predictions aligned with the length of the forecast horizon (fh) set by the sequencer. These predictions constitute the ultimate output of Model 1.

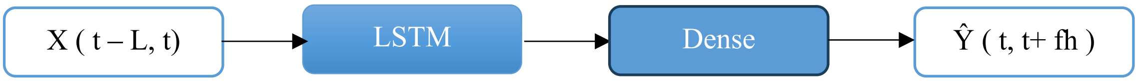

Figure 8: Singular LSTM model with a single layer

3.5.2 Model 2

Model 2, as shown in Figure 8, illustrates a cascade LSTM with two layers of LSTMs in a cascade configuration. All data from geothermal wells and meteorological sources are used as input to LSTM 1. The output of LSTM 1 is then transferred to LSTM 2, and then the output of LSTM 2 is transferred to the dense layer. Responsibility for the sequential processing of the historical data of the past L days, known as the "look-back window", is delegated to the LSTM component. It runs continuously until the present time and produces the final result. The dense layer, in turn, simultaneously generates predictions corresponding to the length of the forecast horizon (fh) specified by the sequencer. These predictions are the final output of Model 2.

Figure 9: Cascade LSTM model

3.5.3 Model 3

Model 3, as shown in Figure 9, is designed with two layers of LSTMs in parallel mode, which are then bonded to a dense layer. The LSTM-1 is responsible for the sequential processing of historical data over the past L days. It runs continuously until the present time, eventually producing the final result. The LSTM-2, on the other hand, manages data for future time points (t + fh), using only the predicted ambient temperature as input at each time step. LSTM-2 returns a complete output sequence based on this input. Note that for the LSTM-2 input, only the sequencer's forecast horizon data is used. Outputs derived from LSTM-1 and LSTM-2 are concatenated and redirected to the dense layer. This dense layer simultaneously generates predictions for elongated time points (t + fh), which serve as the final output of Model 3.

The hyperparameter tuning for this model architecture was conducted concerning prior studies that have extensively examined and optimized hyperparameters for LSTM models in streamflow prediction (Gauch et al., 2021; Kratzert et al., 2018, 2019; Nevo et al., 2022). These studies served as valuable references for fine-tuning the hyperparameters of the model used for predicting warm and cold wells temperatures.

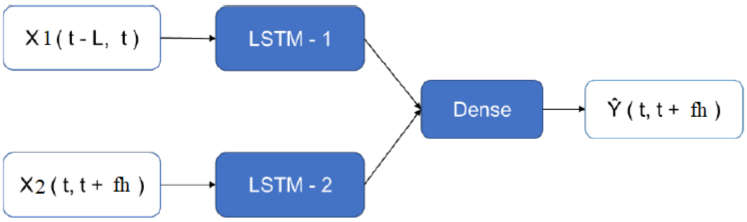

Figure 10: Parallel LSTM model with one dense layer

3.5.4 Model 4

Model 4, as shown in Figure 10, is structured with two parallel layers of LSTM, then bonded to two different dense layers. LSTM-1 is responsible for historical data of the sequencer for the last L days. It worked continuously until the present time finally giving results. In contrast, LSTM-2 processes data for future time points (t + fh) and relies only on predicted ambient temperature as input at each time step. LSTM-2 generates a complete output sequence based on this input, with the caveat that it only uses the sequencer's forecast horizon data for its inputs. The outputs produced by the LSTM-1 and LSTM-2 are concatenated and directed to two separate dense layers. Each of these dense layers is used to predict individual well temperatures. These dense layers simultaneously generate predictions for elongated time points (t + fh), forming the final output of model 4.

The purpose of this model consists of two parts: first, compare the accuracy of its prediction with the previous model, and second, evaluate whether the temperatures of the two wells influence each other.

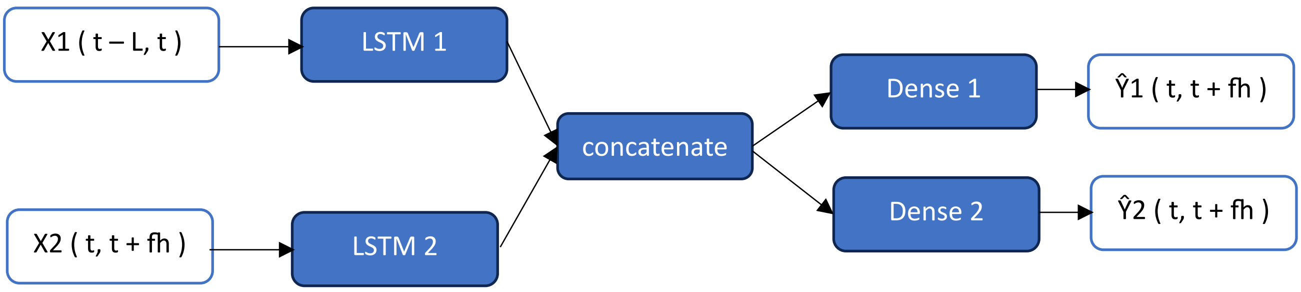

Figure 11: Parallel LSTM model with two separate dense layers

3.6 Data processing

Data analyzing or preprocessing, and post-processing methods and steps used in this study are explained in this session.

3.6.1 Data analyzing or preprocessing

During the data analysis phase, a series of general steps were taken to prepare the data for the DL models. These steps include data visualization, classifying flow direction data, identifying and handling outliers, and resampling data. Splitting data in training, validation, and testing data sets, parameters scaling, and preparation of the sequencer. The following is a detailed explanation of these steps.

3.6.2 Data visualization

In the process of creating long-short term memory (LSTM) models for the analysis of aquifer thermal energy storage (ATES) systems, data visualization plays an important role. This step involves creating visual representations of the ATES system data to gather information, identify patterns, and understand the inherent data structure before using it to train machine learning models such as LSTMs.

The data distribution of the ATES system is explored through data visualization. This is achieved by creating a histogram, box plot, or heat chart to observe how the data is distributed among different features. The goal is to detect any asymmetry, outliers, or patterns in the data. Temporary trends are also detected. Line charts or time series graphs are used to show how system parameters change over time, including temperature fluctuations in hot and cold wells throughout the day or between seasons.

The relationships between different variables are also elucidated through data visualization. This is essential for selecting appropriate features for the LSTM model and evaluating the potential influence of one variable on another. This information serves as a guide for feature engineering, which involves creating new features or transforming existing features to improve model performance. For example, the handling of flow direction data. It makes it easier to interpret model predictions. After training the LSTM model, a comparison is made between its prediction and the actual data, using visualization to assess accuracy and understand possible areas of error. In a nutshell, a comprehensive understanding of data is achieved through data visualization, followed by decisions about data preprocessing, feature selection, and model design. Through data visualization, the LSTM model will be able to have knowledge and proficiency in capturing the underlying patterns and dynamics of the ATES system.

3.6.3 Flow direction classification

Flow direction values range from 0 to 2, including decimals. To prepare this data for inclusion in the ML model and based on information provided by the Koppert-Cress company, a value of 0 means the system is off. Values greater than zero to one indicate a cooling mode in which water is pumped from a cold well to a hot well. Values greater than one to two indicate a heating mode in which water is pumped from a hot well to a cold well. Therefore, flow direction data has been classified into three categories: zero, one, and two for shutdown, cooling, and heating modes respectively.

3.6.4 Outliers identification and replacement

During data visualization, outliers in the data set were identified through the use of a box plot (Figure 11). To deal with the presence of these outliers, a robust approach is taken:

they are replaced by mean interpolation, where neighboring data points are considered for determination. This approach is preferred over eliminating outliers because it retains valuable data and helps maintain the integrity of the data set.

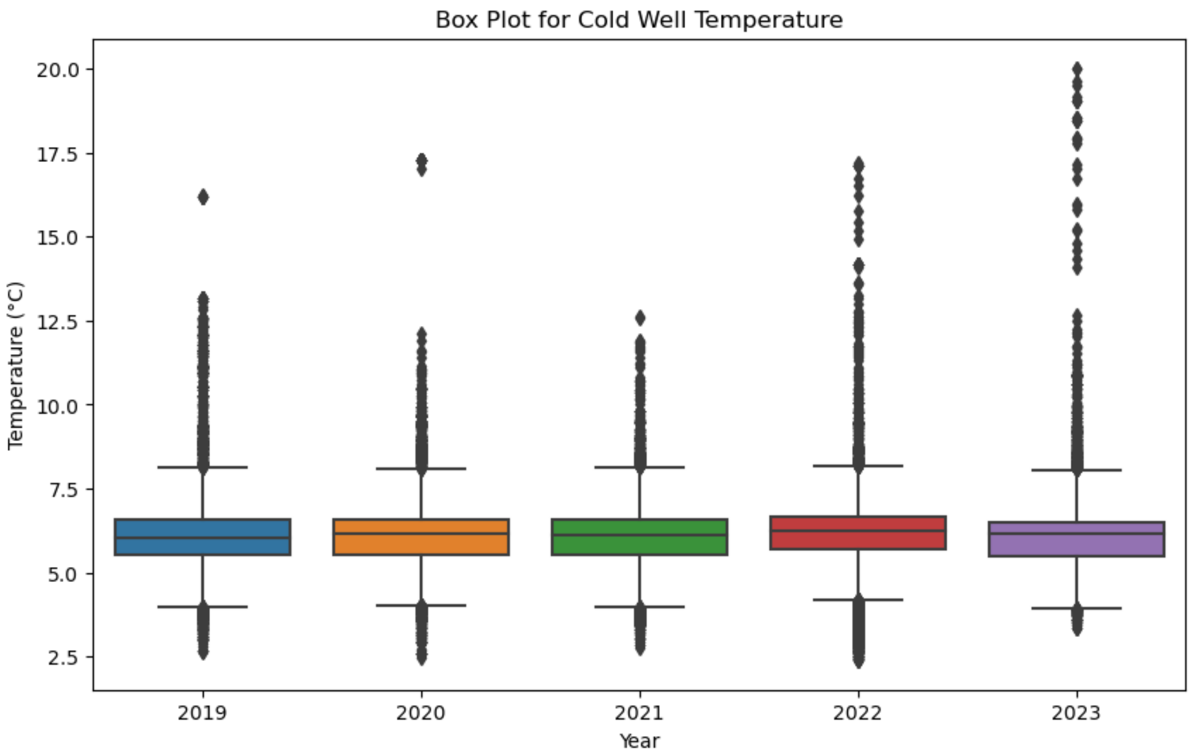

Figure 12: The outliers in the cold well temperature data

3.6.5 Resampling data

Original data are measured at 5-minute intervals. To streamline machine learning training and evaluate prediction accuracy in different scenarios, the data is resampled at different time intervals such as 1, 4, 8, 12, and 24 hours. In Python, there are two separate methods for this purpose: resampling and rolling. The resampling method provides an efficient tool for aggregating data over specified periods, thereby facilitating smoother data management over a while. The rolling method, on the other hand, involves using a sliding window to compute new data points. This approach is particularly useful when performing continuous scrolling data analysis, which is advantageous for tasks such as applying time series smoothing or examining trends over specific periods. The results of the two methods are compared in Figure 12. As seen in the figure the rolling method data has more coverage over the original data.

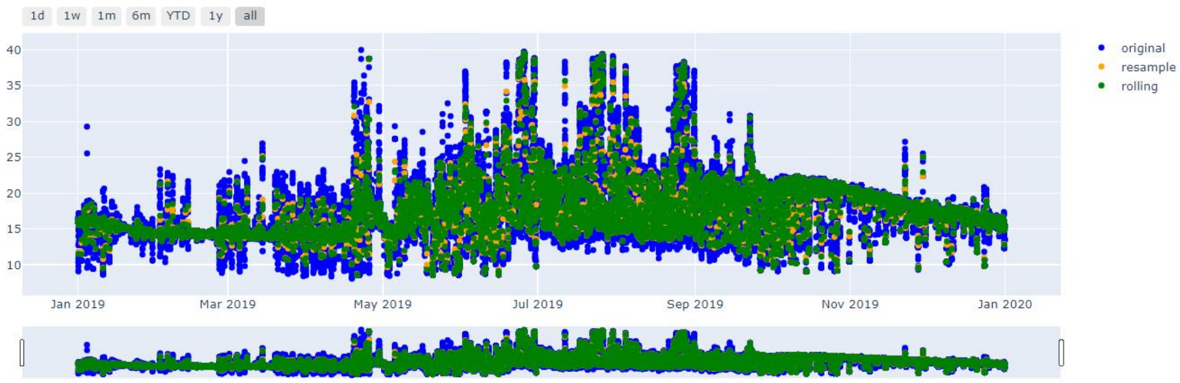

Figure 13: Comparison of resampling and rolling methods results

3.6.6 Data Segmentation for model development and evaluation

The dataset has experienced a cautious division handle, coming about within the creation of three particular subsets: Training, validation, and testing datasets. These subsets have been designated extents of 70%, 15%, and 15% of the whole dataset, respectively. This key division serves as an essential part of the advancement and assessment of machine learning.

1. **Training dataset (70%):**

The biggest parcel, the training set, includes 70% of the dataset. This section plays a principal part in preparing ML models for prediction. By uncovering the demonstration of this broad dataset to the model, it can learn and adjust its inside parameters to capture the fundamental patterns and connections inside the information.

2. Validation dataset (15%):

The validation dataset, comprising 15% of the information, serves as a basic component for fine-tuning the demonstration amid its improvement stage. It acts as an autonomous benchmark for evaluating the model's execution. Alterations to show hyperparameters and design are guided by how well the show generalizes to this dataset.

3. **Testing dataset (15%):**

The testing dataset, to apportion 15% of the information, serves as the extreme assessment ground for machine learning. It gives an impartial evaluation of the model's prescient capabilities on concealed information. The model's execution on this dataset could be a solid pointer to its ability to form exact expectations in real-world scenarios.

This astute apportioning of the information into preparing, approval, and testing subsets guarantees that the ML model is prepared successfully, fine-tuned for optimal execution, and thoroughly assessed for its real-world appropriateness. It could be a pivotal step in building a vigorous and dependable prescient demonstration.

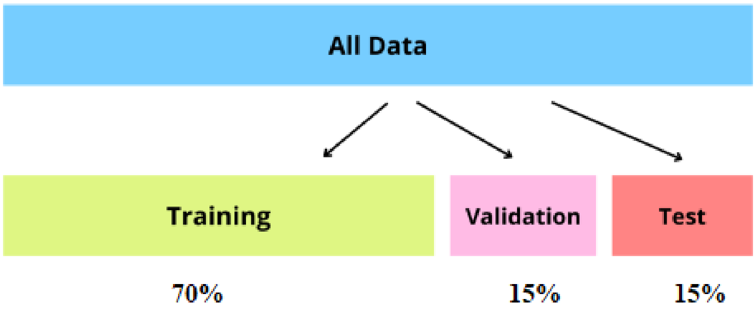

Figure 14: Data proportions

3.6.7 Parameters scaling

In this study, deep learning (DL) models are used to analyze data with multiple input variables, each with a different range of values and units. These variations of the input variables can impact the sensitivity of the model to different factors, potentially leading to a reduction in the model's performance. To mitigate this problem, it is important to apply scaling to the input variables.

The scaling process applied here is normalization. It starts by using the time series data of the input variables specifically for the training dataset. It is essential to emphasize that the scaler is built based on the training dataset only, not including any test or validation dataset. This precaution is taken to avoid any possibility of “data leaks” that could affect the fairness and accuracy of the model evaluation.

From the training data set, the mean $\bar{x}$ and standard deviation σ_x for each input variable are calculated. Then, for each data point in the time series, the normalized value x_{scaled} is calculated using equation 1. The scaler, which encapsulates the mean and standard deviation of each variable taken separately from the training dataset, is stored locally. This standardized scaling method is also extended to the target variable to ensure consistency in the scaling process.

$$x_{scaled} = \frac{x - \bar{x}}{\sigma_x}$$

Equation 1

3.6.8 Preparation of sequences

In the field of time series modeling, sequence preparation plays a central role in efficiently exploiting available data and tailoring it to the unique requirements of the model architecture. select. In the context of this study, we designed two distinct sequence lengths tailored to the specific needs of our model design. These sequence's lengths are as follows:

1- LSTM-1 string length (look-back window):

A sequence length is specified for LSTM-1. This particular length serves as a "look-back window" for LSTM-1, allowing the model to take into account important historical context when making predictions.

2- LSTM-2 series length (forecast horizon):

In contrast, the LSTM-2 (or second group of LSTMs). In this case, the length of the series corresponds to the "forecast horizon" of LSTM-2, allowing the model to make shorter-term predictions with a more focused view of recent data.

To provide a visual representation of this sequence preparation procedure, you may refer to Figure 14, which shows a diagram detailing how these sequences were constructed and aligned with the parallel model architecture. This preparatory step ensures that our models are optimized to efficiently capture and exploit temporal patterns in the data, meeting the unique requirements of each LSTM variant.

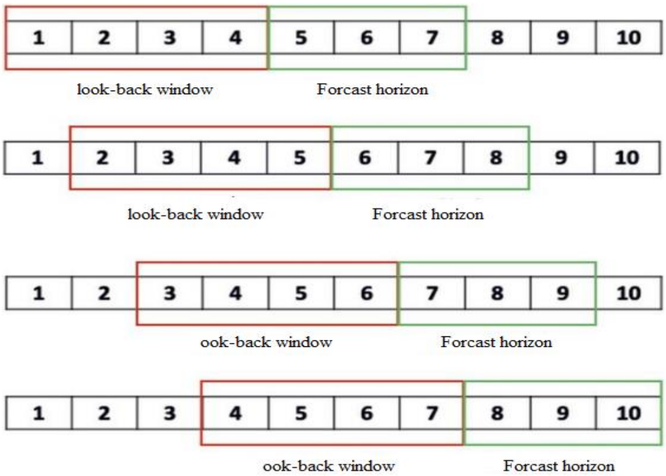

Figure 15: Sequencer setup. "look-back window" data is separated for LSTM1 and "forecasting horizon" is divided or LSTM2

3.6.9 Postprocessing

In the post-processing stage, some essential processes are performed to process the predicted values. These processes include tasks such as back-scaling predicted values, visualization, and comparative analysis with the original data.

3.6.9.1 Back-scaling predicted values

During the preprocessing stage, the target variable (the predicted values) undergoes scaling, producing normalized values denoted by y_{scaled}. To achieve this normalization, we calculate the mean $\bar{y}$ and standard deviation σ_y of the observed target variable using the training dataset. We then use the scaler to reverse the transition, ensuring that the modeled target is scaled back to the original scale, as adjusted by Equation 2.

$$y = y_{scaled} \times \sigma_y + \bar{y}$$

Equation 2

3.7 Evaluation metrics for long short-term memory (LSTM) Model results

3.7.1 Mean absolute error (MAE)

Definition: The MAE calculates the average size of errors between actual and anticipated values. It is determined by first averaging the absolute disparities between each anticipated value and its matching actual value.

Interpretation: A lower MAE means that, on average, the model's predictions are more in line with the actual data. Compared to other metrics like MSE, it is less susceptible to outliers.

$$MAE = \frac{\sum_{i=1}^{n} \left| \hat{Y}i - Yi \right|}{n}$$

Equation 3

3.7.2 Mean squared error (MSE)

Definition: MSE also looks at prediction errors but squares them before averaging. This makes it more sensitive to large errors.

Interpretation: Like MAE, we want a lower MSE. It emphasizes big mistakes more, so it's crucial to minimize this if outliers are significant.

$$MSE = \frac{1}{n}\sum\nolimits_{i=1}^{n}\left(Yi - \hat{Y}i\right)^2$$

Equation 4

3.7.3 Root mean squared error (RMSE):

Definition: RMSE is just the square root of MSE. It's useful because it gives us an error measurement in the same units as our data, making it easier to understand.

Interpretation: Similar to MSE, we aim for a smaller RMSE for more accurate predictions.

$$RMSE = \sqrt{\frac{\sum_{i=1}^{n}\left(Yi - \hat{Y}i\right)^2}{n}}$$

Equation 5

3.7.4 Coefficient of determination (R^2 or R-squared):

Definition: R^2 tells us how well our model fits the data. It ranges from 0 to 1, where 0 means our model is not useful, and 1 means it's a perfect fit.

Interpretation: Higher R^2 values are better. They indicate that our model explains more of the variation in the data. It helps us understand how well our predictions align with reality.

$$R^2 = 1 - \frac{RSS}{TSS}$$

$$RSS = \sum_{i}^{N}(y_{predicted} - y_{measured})^2$$

$$TSS = \sum_{i}^{N}(y_{measured} - y_{mean})^2$$

Equation 6

Results

The results will be presented and discussed in this chapter in two sections: section 4.1 illustrates the data visualization and findings, and section 4.2 compares the performance of different LSTM model architectures. Each section addresses a sub-research question, first presenting the results and findings, followed by a discussion.

4.1 Data visualization

4.1.1 Cold and warm well temperature comparison during heating and cooling mode.

Distinct patterns are revealed in the operation of the ATES when operating in both cooling and heating modes. In the visualization, the cooling mode is represented by blue data points, while the heating mode is indicated by red data points. Valuable information about the thermal characteristics of the system is provided by the observed temperature dynamics in these modes.

During the cooling cycle, higher temperatures are normally detected at warm wells. This phenomenon is due to the ATES system absorbing excess heat from the building during this period. Efficient heat transfer by the heat pump allows this heat to be stored in the water. The heat-rich water is then pumped into the warm well, contributing to the increase in the temperature of the warm well (Figure 15).

In contrast, when the system is in heating mode, the temperature in the cold well is usually lower. This property is the result of extracting heat from the water in the system to heat the building. Therefore, the water temperature decreases during this period. To restore balance, cooler water is pumped into the cold well, helping to lower the temperature (Figure 16).

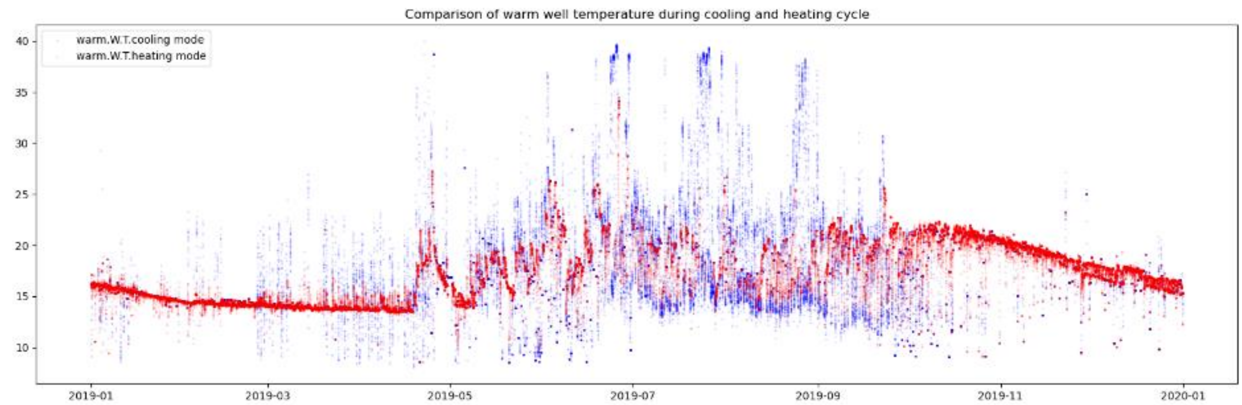

Figure 15: The warm well experiences a higher temperature during building cooling mode because of absorbing heat from the building and storing warm water inside the warm well.

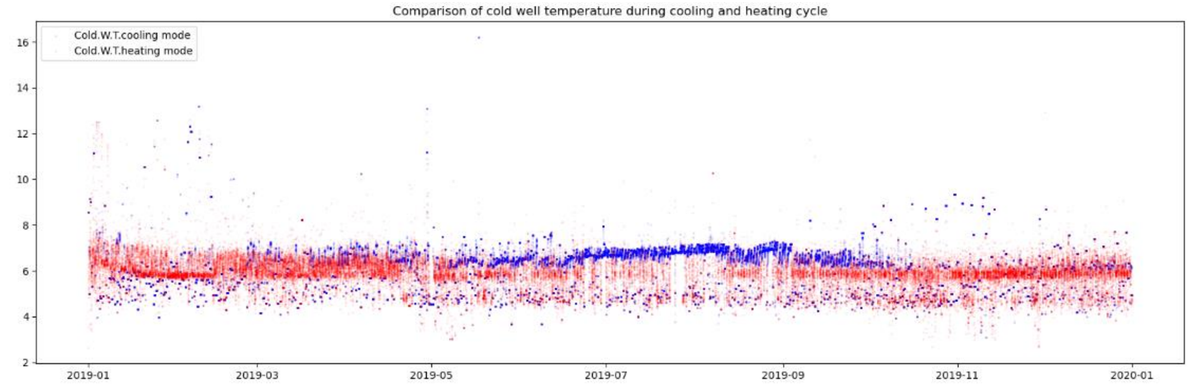

Figure 16: The cold well experiences a lower temperature during building heating mode because of leaves its heat to the building and stores cold water inside the cold well.

4.1.2 Flow direction

As mentioned in the methods section, flow direction values range from 0 to 2, including decimals. In this context, the value zero corresponds to the system shutdown period. Values greater than zero to one indicate cooling mode, while values greater than one to two indicate heating mode. Figure 17 illustrates that the heating mode accounted for 37.7% of the total duration, while the cooling mode accounted for 22.8%. This allocation indicates a higher heating demand, underscoring the importance of prioritizing heating mode in the system.

About 68.9% of the time, the system operates in modes 0, 1, or 2, reflecting its typical operating states. The remaining 31.1% can be attributed to the transition period between cooling and heating modes, providing valuable opportunities for measurement and data analysis.

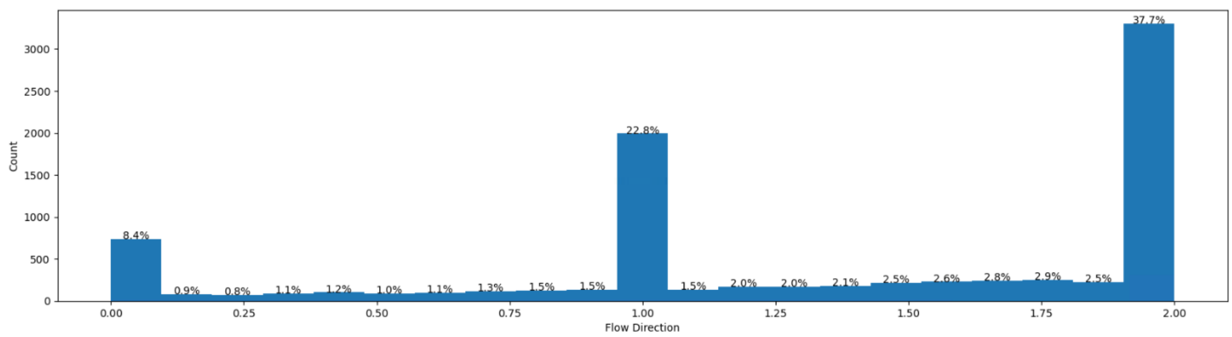

Figure 16: 37.7% of the time in heating mode and 22.8% of the time in cooling mode. Emphasizing on heating mode of the system. The system operates within modes 0, 1, and 2 for 68.9% of the time, with 31.1% as transitional periods.

To streamline the data analysis process, a classification scheme has been introduced to categorize flow direction data into three distinct classes:

1. The designation “0” signifies periods of system shutdown.

2. Values within the range of 0 to 1 have been replaced with number "1" to represent the cooling cycle.

3. Values exceeding 1 to 2 are replaced with the number "2" and employed to denote the heating mode.

This classification methodology has been implemented to enhance the clarity and manageability of data analysis, ensuring that flow direction data can be readily interpreted and comprehended within the defined categories.

4.1.3 Correlation between flow direction and wells' temperatures

Figure 18 illustrates the schematic of ATES wells, sensor locations, and the heat exchanger in the Koppert Cress ATES system.

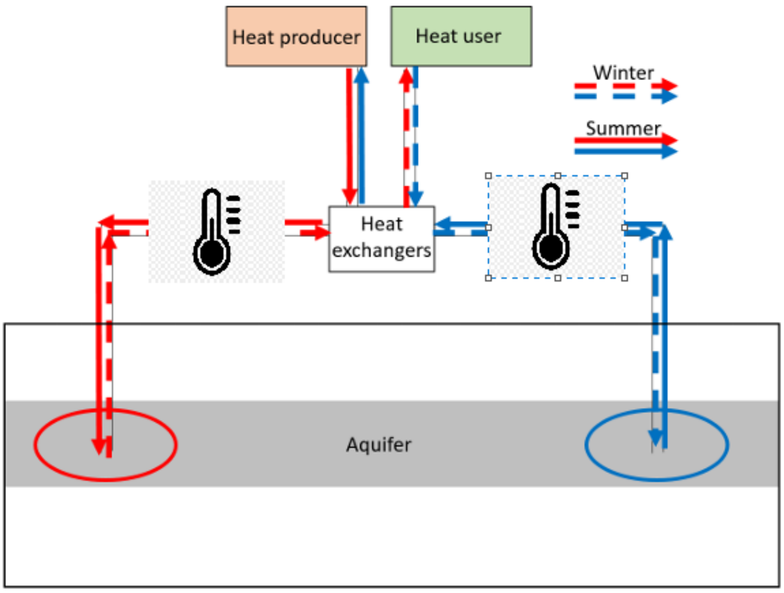

Figure 17: Schematic of ATES wells, sensor locations

The most pronounced temperature fluctuations occur within the water discharged from the heat exchanger, as it undergoes energy gain or loss within the heat exchanger (HE). In contrast, the HE tends to maintain a relatively stable temperature profile. This consistency arises from its source within the well, where the temperature remains relatively constant over time.

Figure 19 illustrates that, within each cooling or heating cycle, the temperature fluctuations are more pronounced in the injection water supplied to the well compared to the temperature of the produced water from the well. This disparity is particularly evident in modes lasting over five hours.

The impact of the cooling mode on the warm well temperature (or injection water temperature) is most conspicuous during June and July, primarily due to the longer duration of the cooling mode in comparison to the heating mode during this specific period.

Typically, the highest temperatures are recorded at the onset of the cooling phase, coinciding with the initiation of the heat pump`s cooling operation for the building. During this phase, the water within the heat exchanger absorbs the maximum amount of heat. Subsequently, as the cooling mode progresses and transitions into the heating mode, the heat pump progressively reduces its heat absorption by the water.

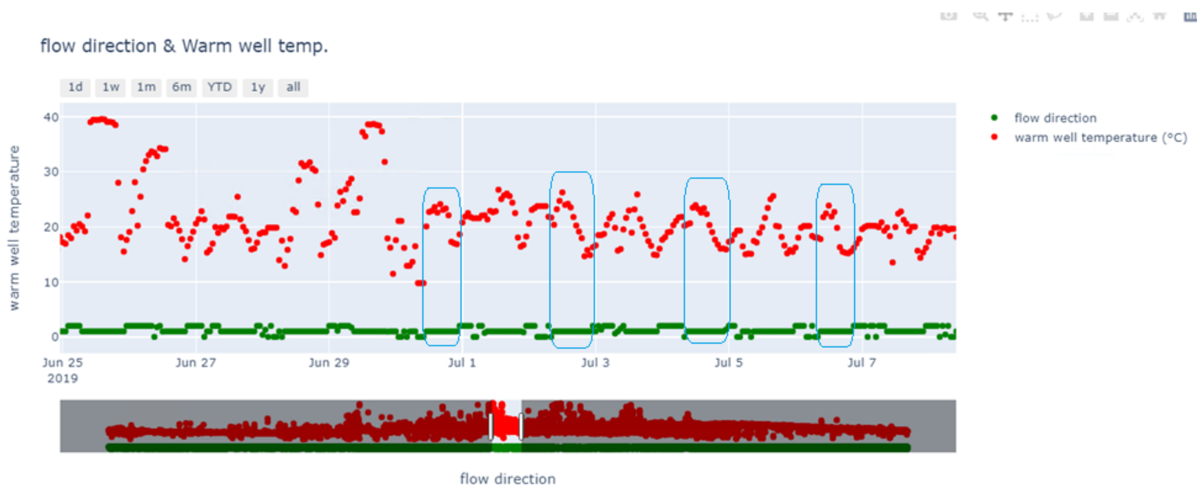

Figure 18: More temperature variation is experienced in injecting water into wells in comparison to extracted water from wells. Cooling mode impacts warm well temperature mostly during June and July, with peak temperatures at the start of the cooling phase.

The amount of heat absorbed by the building depends on the temperature requirements inside the structure. The degree of temperature fluctuations during a cooling cycle is closely related to the energy needs inside the building. The main goal of the HVAC system is to maintain a stable indoor temperature. Therefore, when the inside of the building is warmer, the heat exchanger (HE) will absorb higher temperatures, while the lower building temperature causes the HE to absorb cooler temperatures, all of which are of concern to the public. temperature stability. (figure 20)

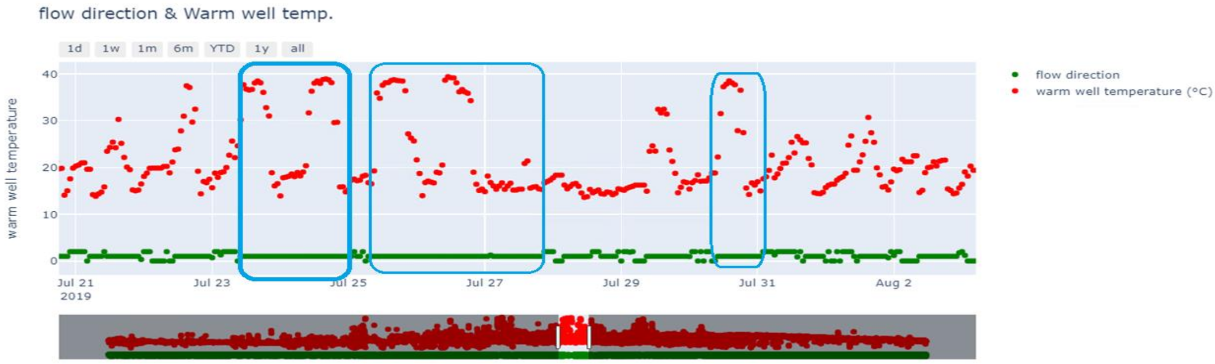

Figure 19: Heat Exchanger adapts to building temperature demands, which leads to absorbed temperature fluctuations during cooling cycles, for maintaining consistent temperatures inside the structure.

In the earlier discussion during the cooling mode temperature variation was explained, it follows that during the heating mode too. When water is injected into the cold well, the most significant temperature fluctuation (resulting in the lowest temperature reading) is expected to be observed at the cold well. This is in line with the dynamic temperature adjustments characteristic of the ATES system`s operation. (figure 21)

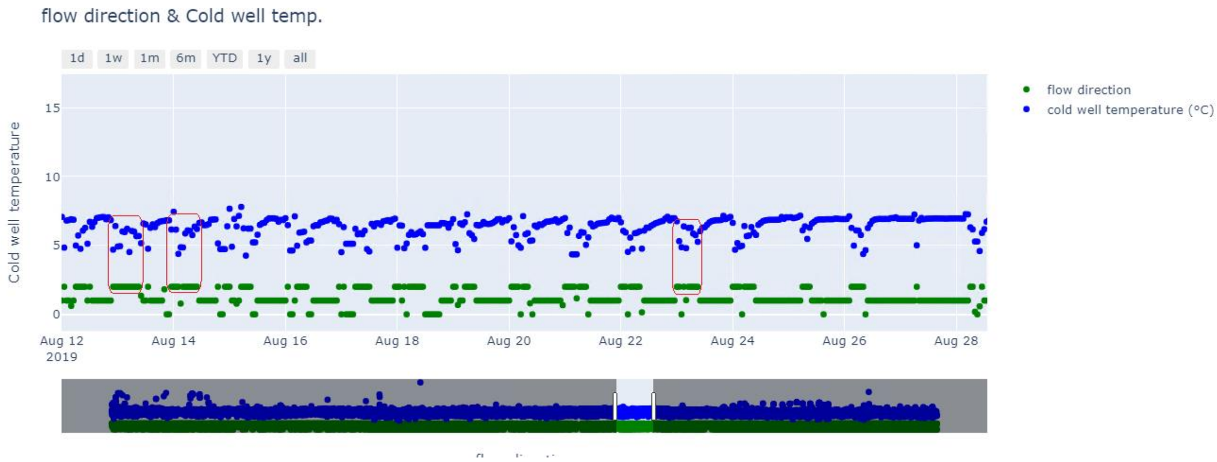

Figure 20: In the heating mode, when cooler water is injected into the cold well, the coldest temperatures are detected by the cold well sensor.

4.1.4 Correlation between environmental temperature and the flow direction

When environmental temperature and flow direction are compared together, clear patterns emerge. The system typically works in heating mode when the outside temperature is below ten degrees (figure 22). The system switches into cooling mode when the ambient temperature progressively increases. In contrast, the system switches back to heating mode as the temperature drops (figure 23).

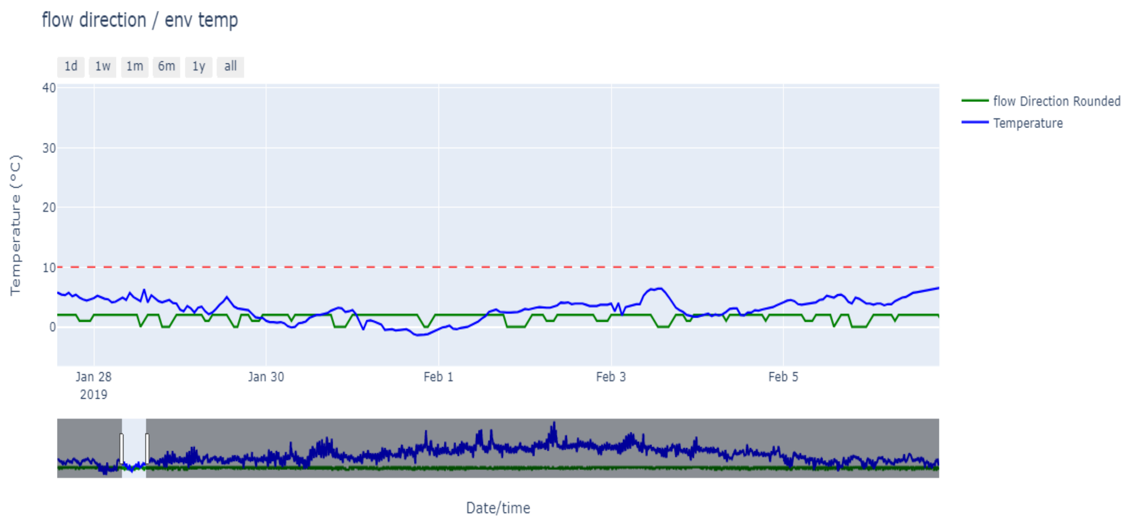

Figure 21: The system predominantly operates in heating mode when the exterior temperature remains below 10 degrees

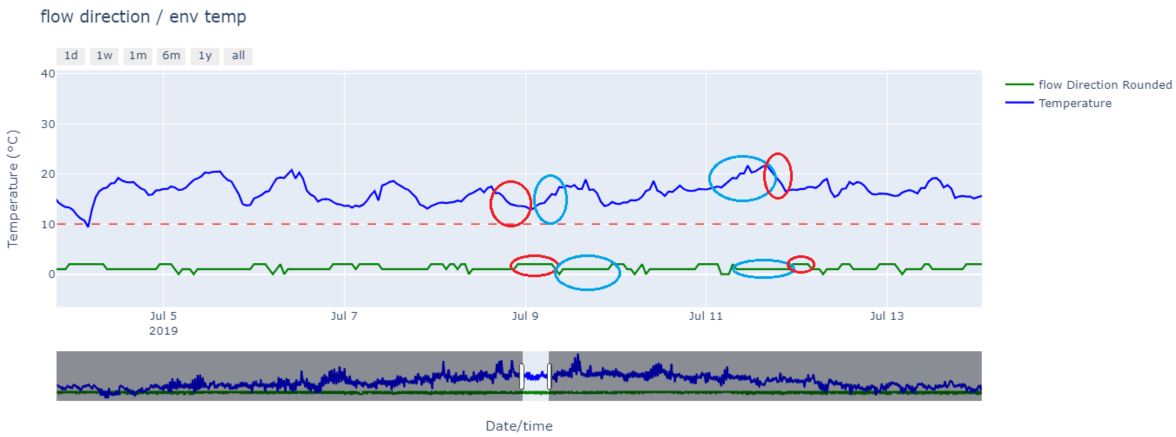

Figure 22: when the ambient temperature progressively increases the system switches into cooling mode. In contrast, the system switches back to heating mode as the temperature drops.

4.1.5 Correlation between environmental temp and warm well temperature

The comparison of temperature variations between the environment and well temperatures reveals intriguing correlations. Typically, there is a robust correlation between warm well temperature and environmental temperature, particularly when the environmental temperature exceeds fifteen degrees. Under such conditions, these two graphs tend to align closely. However, it's noteworthy that in some instances, the warm-well temperature surpasses the maximum environmental temperature. This occurrence can be attributed to additional heat sources such as solar panels, and neighboring company's waste water heat that impart extra energy to the water, thus elevating the warm well temperature.

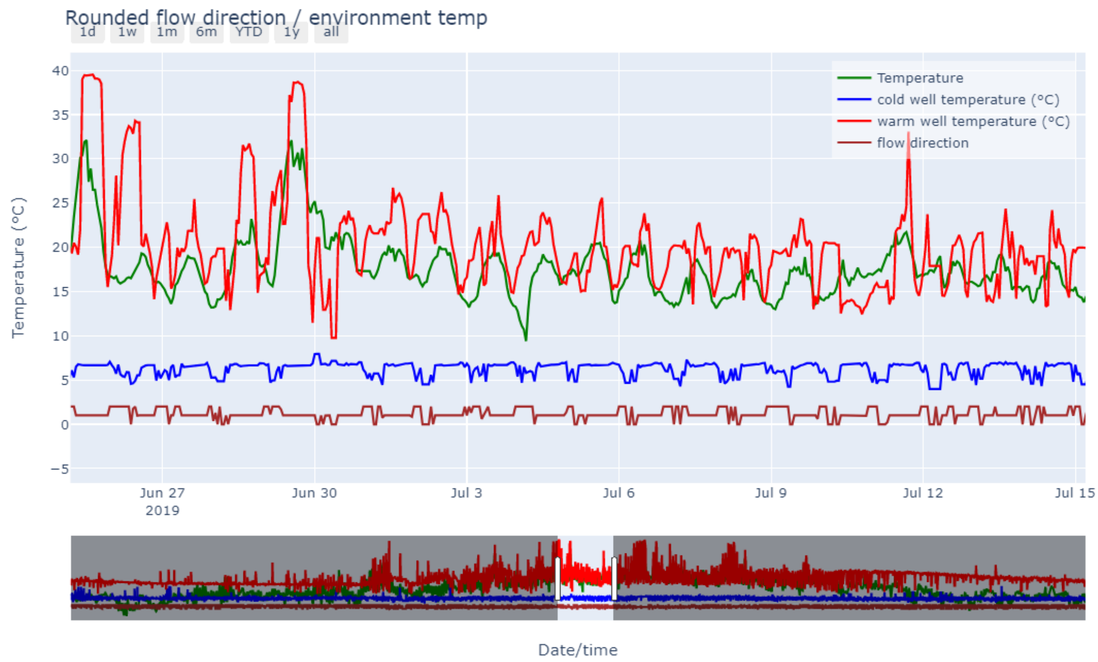

Figure 23: A strong correlation is observed between warm well temperature and environmental temperature, especially when the latter exceeds 15 degrees.

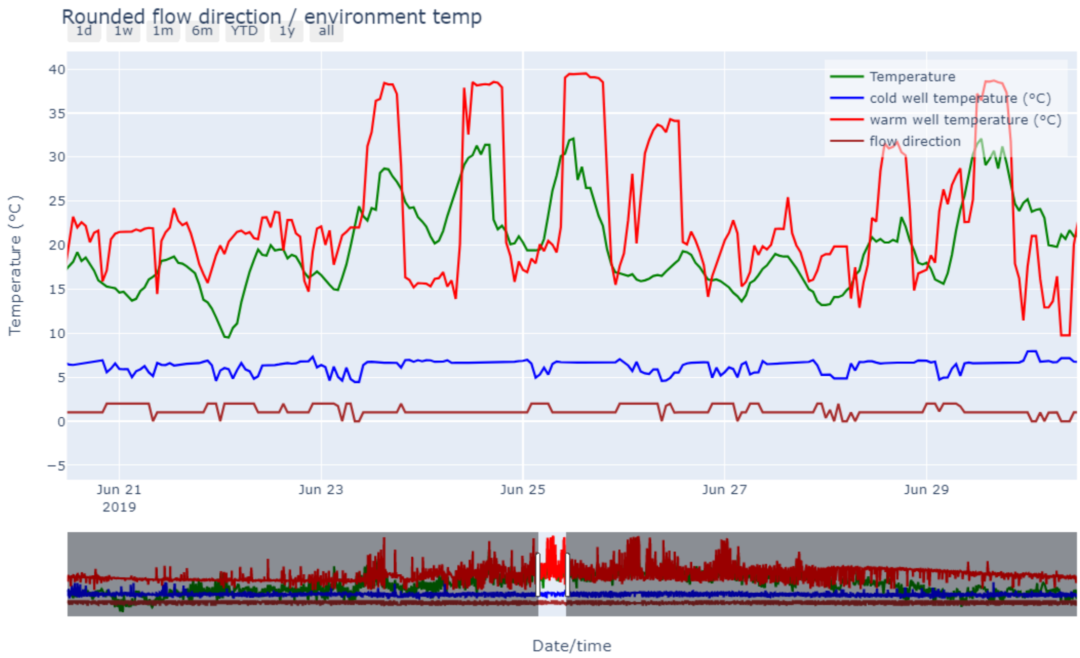

Figure 24: The warm well temperature occasionally exceeds the highest recorded environmental temperature. This phenomenon can be ascribed to supplementary heat sources, such as solar panels and waste heat from neighboring companies.

4.1.6 Correlation between environmental temp and cold well temperature

On the other hand, it's important to note that when it comes to cold well temperature and their relationship to ambient temperature (figure 26), the odd absence of any clear and consistent relationship is noticed. This interesting lack of correlation can be unraveled by examining the basic principles that govern heat pumps when operating in cooling mode, as well as the limitations imposed by extremely low temperatures.

When the heat pump is in heating mode, its main purpose is to transfer heat from the water to the inside of the building, thereby cooling water. This process involves the circulation of a heat transfer fluid, usually water, through a series of coils and pipes. However, it is important to keep the water temperature above a certain threshold, usually around 5 degrees, to avoid the risk of freezing in the heat pump condenser. The need to prevent freezing in the heat pump system at extremely low temperatures places a limit on the temperature of the cooler. This limitation can create a disconnect between the cold well temperature and the ambient temperature. Even when the outside environment has a significant drop in temperature, the heat pump will work to maintain the cold well temperature within a certain range, ensuring that the temperature remains above the critical freezing point.

This unique behavior demonstrates the adaptability and intelligence of heat pump systems in managing temperature variations and maintaining the safety and efficiency of their operations. So while it may seem counterintuitive to suggest that the cold well temperature does not consistently reflect the ambient temperature, it is evidence of the complex engineering and control mechanisms that underlie the operation. behavior of heat pumps, especially when 'they are deployed for cooling purposes.

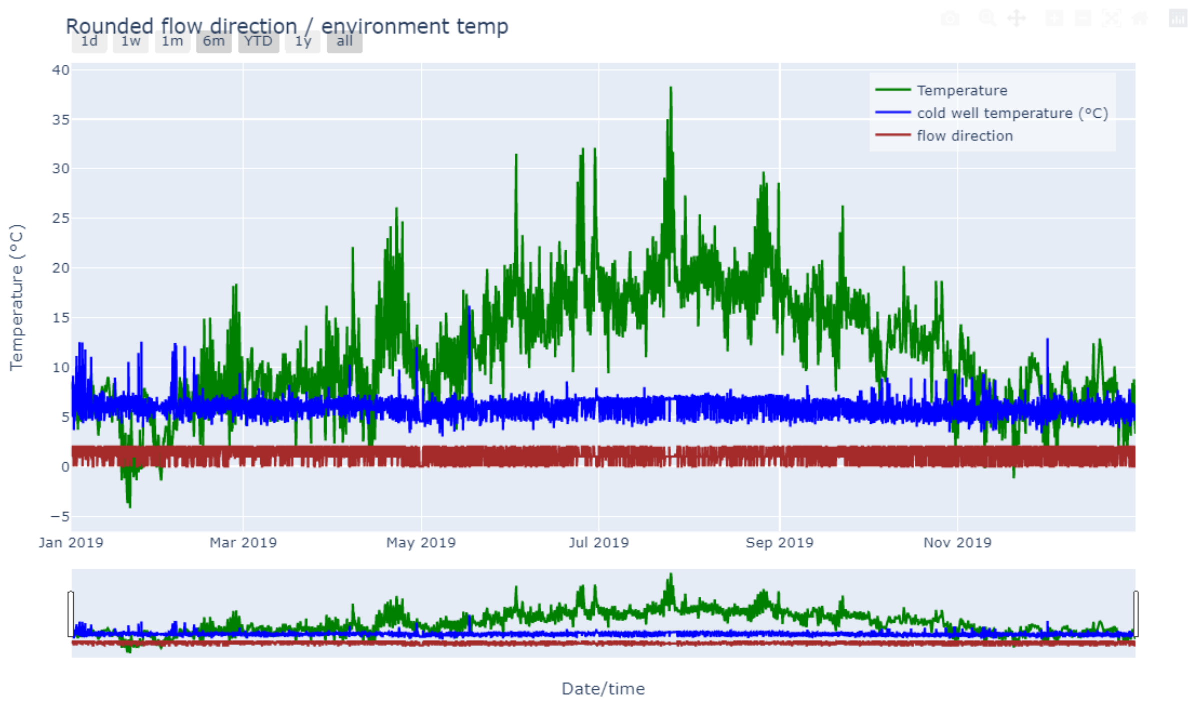

Figure 25: The cold well temperature and environmental temperature comparison.

4.1.7 Data outliers and abnormalities, and their Management

During data analysis, two distinct categories of outliers were encountered.

4.1.7.1 Sensing errors

The first category was related to sensor locations (figures 27 & 28 & 29). After a careful review of the source data and a comparison with similar timeframes in other years, as well as the creation of visual plots, the underlying reasons for these anomalies were identified.

It was observed that these outliers were associated with the placement of the sensors themselves. It should be noted that the sensors are not positioned within the wells; instead, they are strategically installed somewhere between the heat pumps and the wells. Consequently, the function of monitoring the temperature of the water as it exits or enters the wells is carried out by them.

Several factors can contribute to the emergence of outliers in this context. For instance, when the system undergoes temporary shutdowns or switches between cooling and heating modes, the flow of water can momentarily cease. During these periods of flow interruption, temperature fluctuations either cooling down or heating up are experienced by the water within the pipes. These fluctuations are duly detected by the sensors, and these variations are recorded and stored in the dataset.

Therefore, it is crucial to recognize that these recorded numbers do not represent the true temperature of the wells themselves. Instead, the transient changes in water temperature as it is moved through the system are reflected by them. As a result, any analysis or interpretation of the data must take into account the nature of these sensor readings and their underlying causes, rather than treating them as authentic representations of the actual well temperatures.

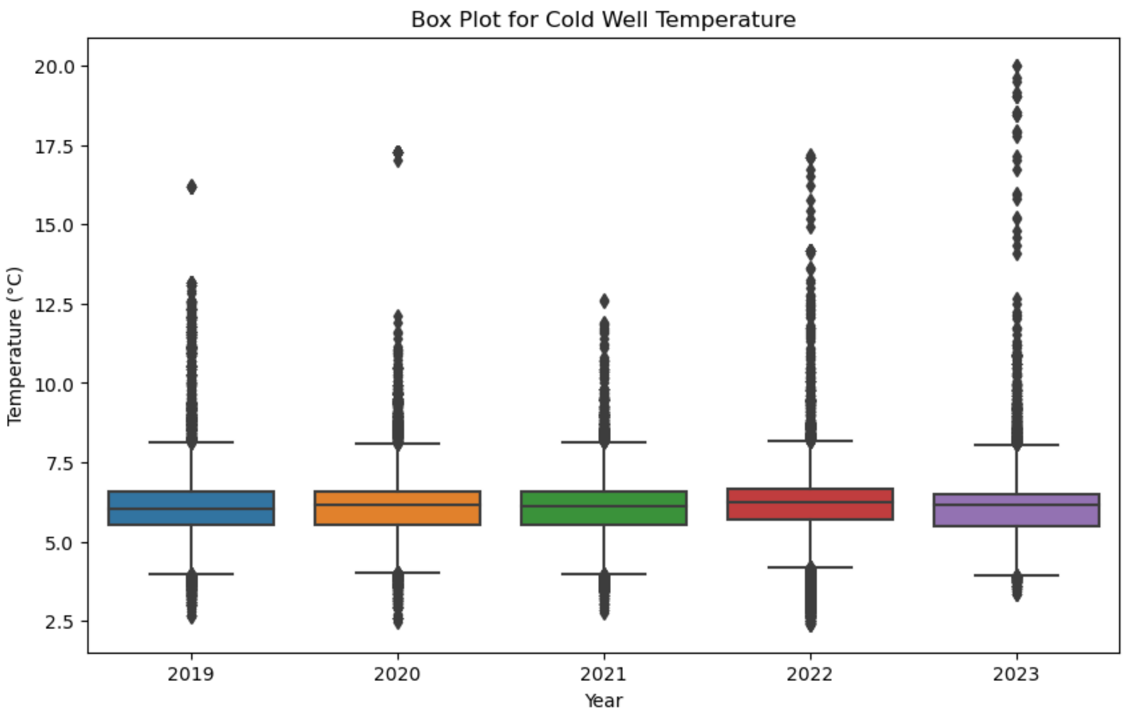

Figure 26: Cold well outliers

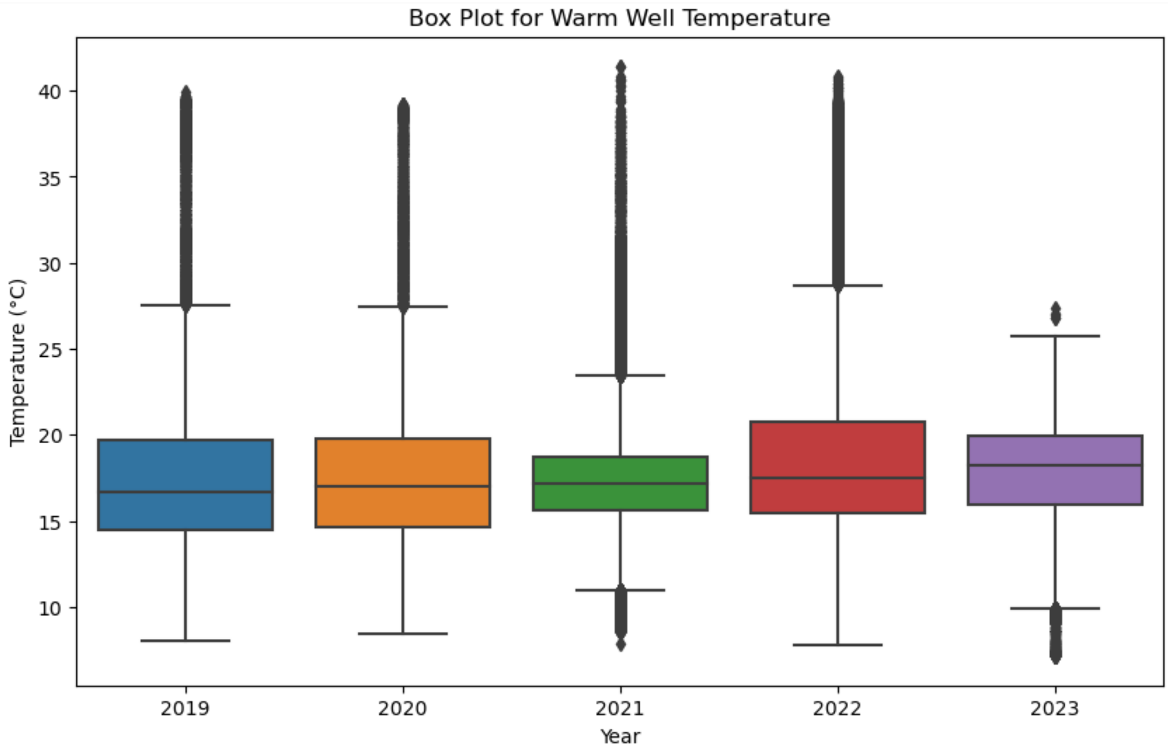

Figure 27: Cold well outliers

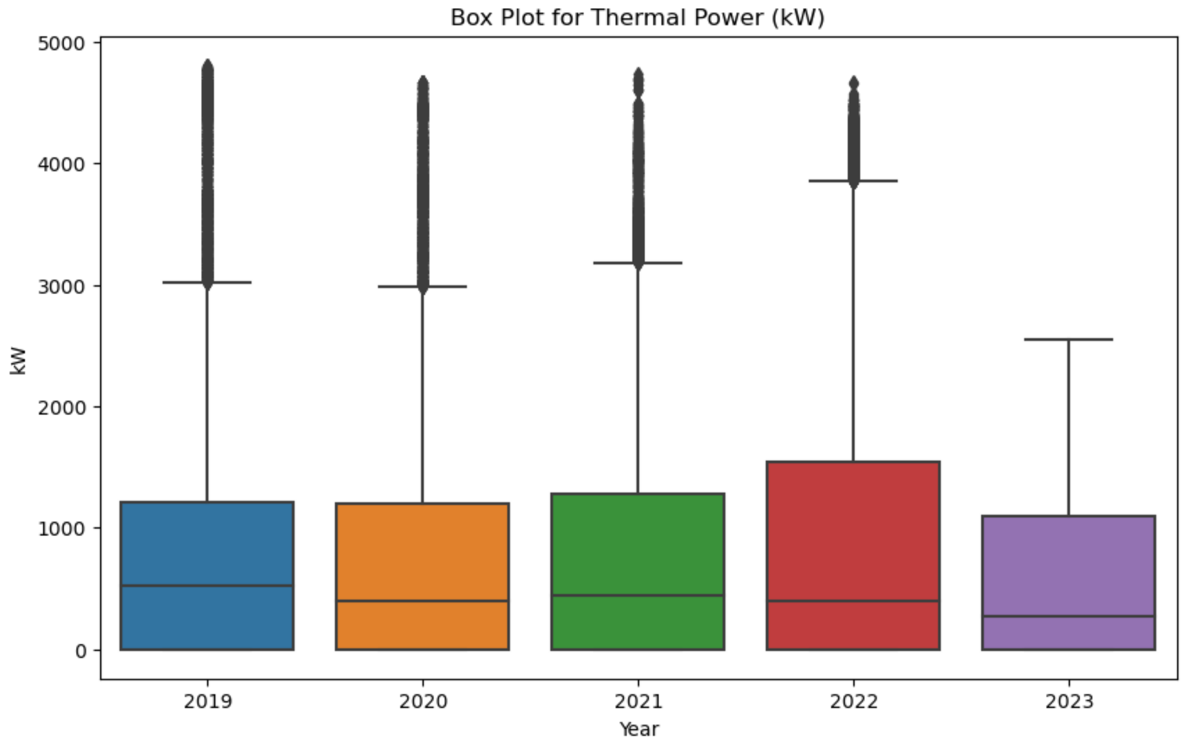

Figure 28: Cold well outliers

4.1.7.2 Cable malfunction

The second category of data anomalies pertained to a specific period in 2020 when warm well temperatures were recorded to be exceeding 100 degrees, while cold well temperatures surpassed 65 degrees. These readings sharply contrasted with the typical temperature ranges observed in the wells, where the maximum temperature for warm wells usually hovers around 40 degrees, and for cold wells, it stays at approximately 12 degrees. Further investigation revealed that this unusual data was a result of a cable malfunction that occurred on that particular day, leading to the erroneous recording of these abnormal temperature values (see Figures 4.16 & 4.17).

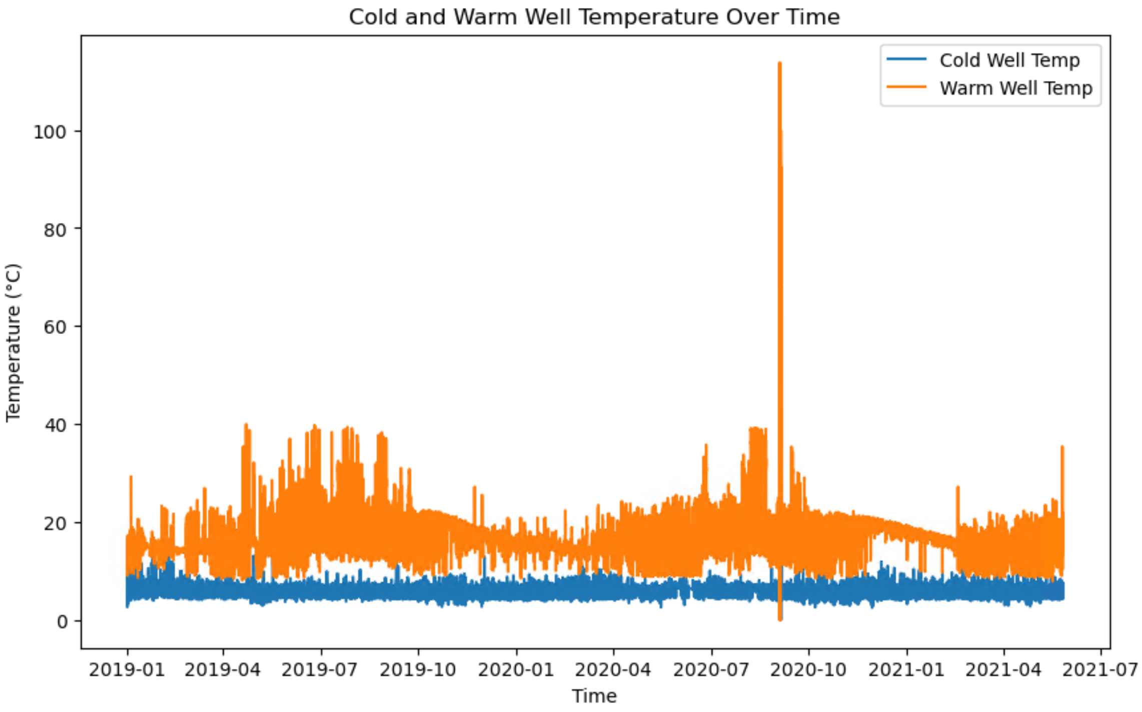

Figure 29: Warm and cold wells abnormalities

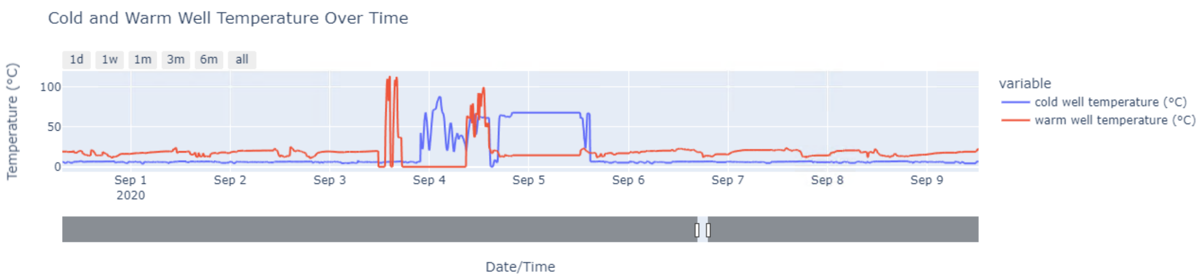

Figure 30: The exact time of abnormities and their amounts

Also, similar abnormalities were seen in flow rates (Figures 4.18 & 4.19).

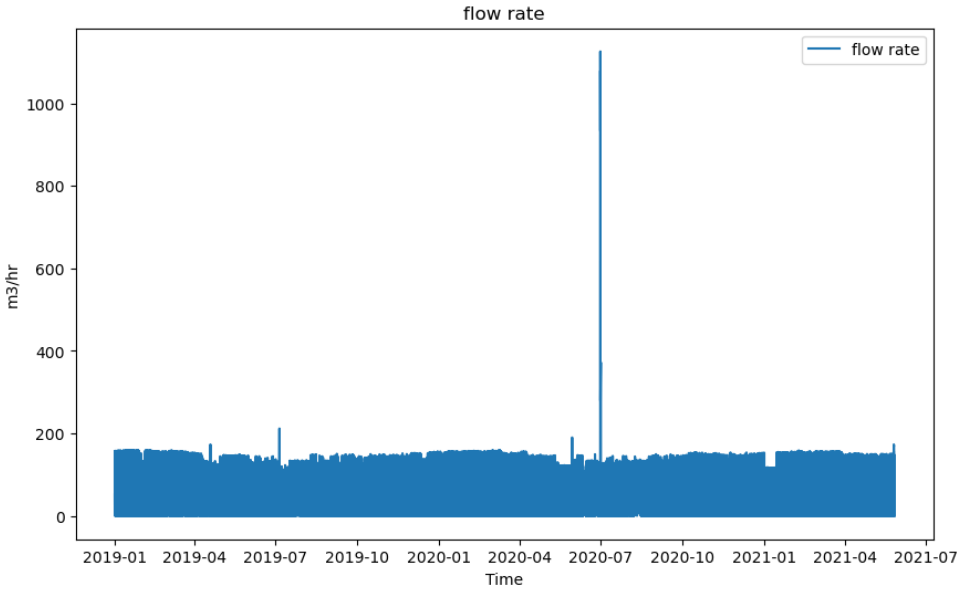

Figure 31: flow rate abnormalities

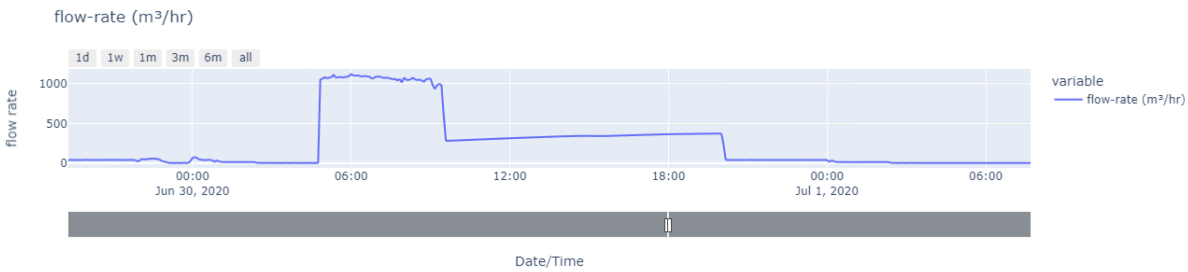

Figure 32: Exact time of abnormities and their amounts

4.2 LSTM models results

As a comprehensive detail, before attending to the LSTM models' results it is fundamental to note this ATES system started in 2012 up to the present day. Over these years, various changes have happened, such as the transition from LT-ATES to HT-ATES in 2015, the presentation of a pond in 2016, solar panels, and waste heat from a neighboring combined heat and power (CHP) plant in 2017, and the expansion of a cold store in 2018.

Consequently, it becomes evident that the system experienced significant transformations during this period. Therefore, as observed after this transitional phase, the data started to exhibit a greater degree of stability. Consequently, a decision was made to utilize data from this post-transition period onwards. This decision was driven by the objective of minimizing uncertainties in the dataset. Thus, data spanning from 2019 to the present has been employed for analysis and modeling.

4.2.1 Singular LSTM model

Initially, the singular LSTM model was implemented in the dataset. After some hyper-parameter adjustments, optimal results were obtained with 12-hour resolution data. Then a systematic process was applied, in which the resolution of the data was gradually increased. over 8 hours and 4 hours, and finally applied a data usage model with a resolution of 5 minutes.

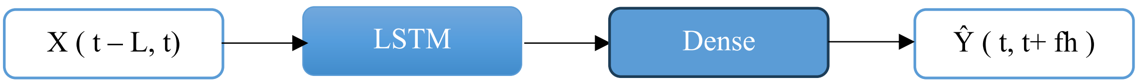

Figure 33: Singular LSTM model

4.2.1.1 Singular LSTM model, for predicting one feature (warm well temperature)

4.2.1.1.1 Singular LSTM model, for predicting one feature (warm well temperature in) at 12 hours data resolution

The outcomes of this experiment, which evaluates the model's execution through the convergence plot comparing training loss and validation loss based on mean squared error (MSE), are illustrated in Figure 35. The x-axis shows the epochs of iteration, while the y-axis illustrates the value of the evaluation metrics (loss function) of training data. After 8 epochs training of the model starts to stabilize. As the early stop function is used inside of the LSTM model training stops after 34 epochs to prevent overfitting the model.

Besides, Figure 36 presents key measurements, where MSE stands at 4.10, RMSE at 2.02, R-squared (R^2) at 0.06, and MAE at 1.58.

These measurements uncover that the model is competent in capturing the general temperature variation for forecast, although it battles to imitate it. Figure 37 outwardly illustrates this by exhibiting the comparison between the real temperature values (in blue) crossing nine months and the comparing predicted values (in orange).

Figure 38 gives a comprehensive diagram, enveloping training, validation, test, and predicted values.

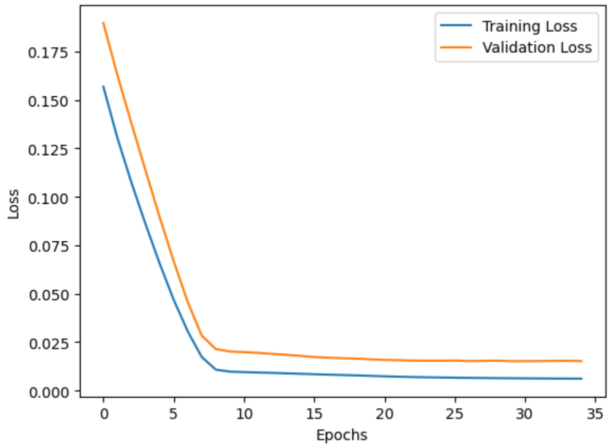

Figure 34: Convergence plot of training and validation losses

```
MSE for Warm Well Temperature: 4.10271855463773

RMSE for Warm Well Temperature: 2.0255168611092156

R-squared for Warm Well Temperature: 0.1699535921873374

MAE for warm well: 1.5872441005416964
```

Figure 35: ML model evaluating metrics

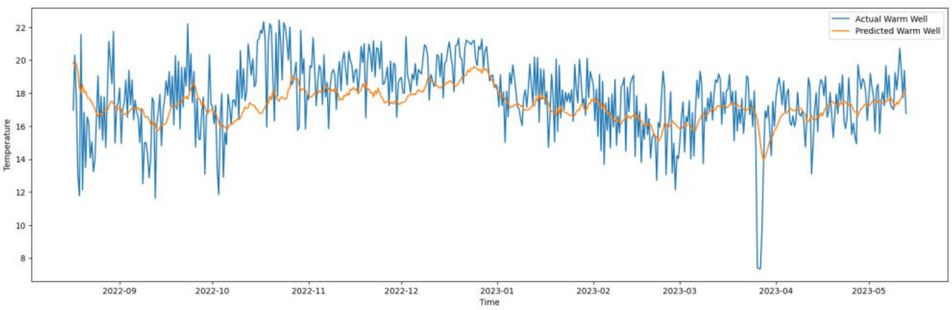

Figure 36: Actual and predicted temperatures for warm well

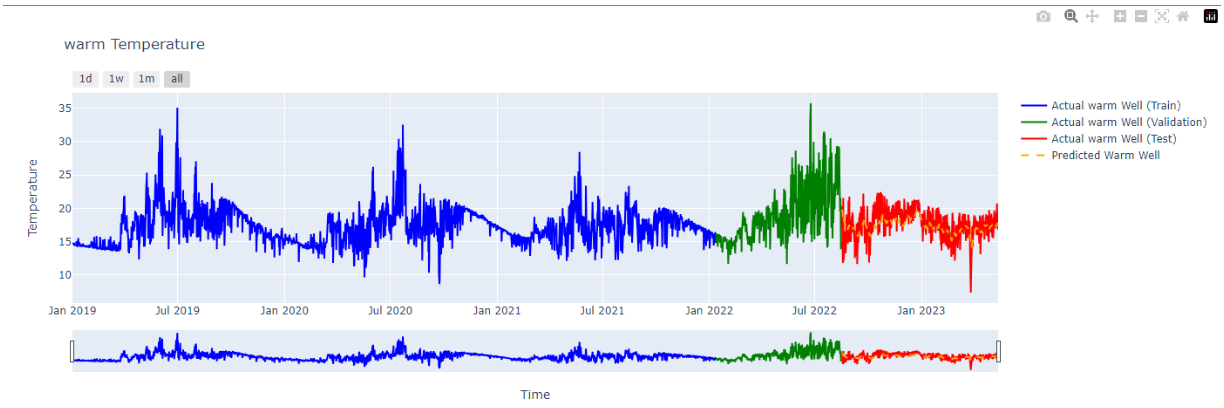

Figure 37: Training, validation, test, and prediction values of warm well temperature

4.2.1.1.2 Singular LSTM model, for predicting one feature (warm well temperature in) at 8 hours data resolution

The results of this experiment, which assesses the model's performance using a convergence plot that compares training loss and validation loss based on Mean Squared Error (MSE), are depicted in Figure 39. Additionally, Figure 40 presents key performance metrics, with MSE recorded at 4.63, RMSE at 2.15, R-squared (R^2) at 0.20, and MAE at 1.66.

These metrics reveal that the model is proficient in capturing the overall temperature variation for forecasting, albeit with some limitations in accurately reproducing it. This is visually evident in Figure 41, which illustrates the comparison between the actual temperature values (in blue) spanning nine months and their corresponding predicted values (in orange).

For a more comprehensive overview encompassing training, validation, test, and predicted values, please refer to Figure 42.

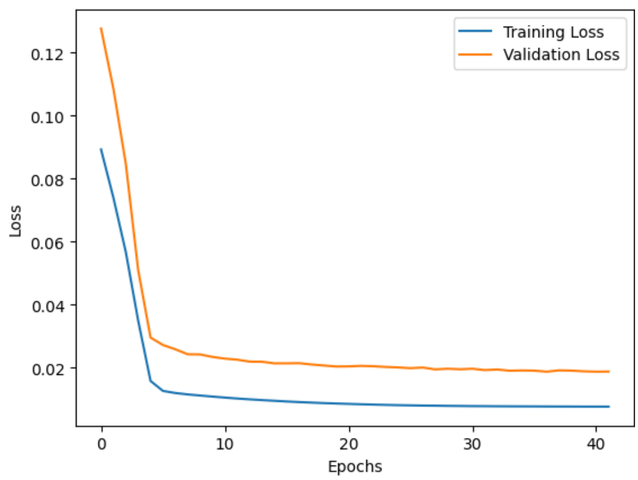

Figure 38: Convergence plot of training and validation losses

```
MSE for Warm Well Temperature: 4.638803728070032

RMSE for Warm Well Temperature: 2.15378822730324

R-squared for Warm Well Temperature: 0.2040466947538716

MAE for warm well: 1.6608682489730917
```

Figure 39: ML model evaluating metrics

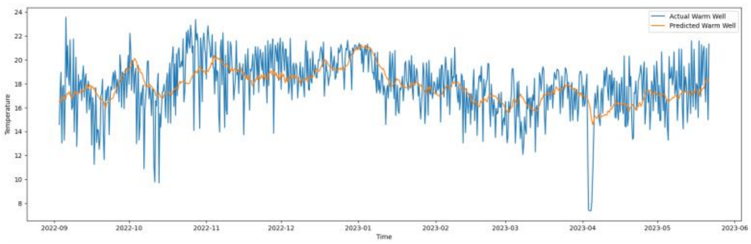

Figure 40: Actual and predicted temperatures for warm well

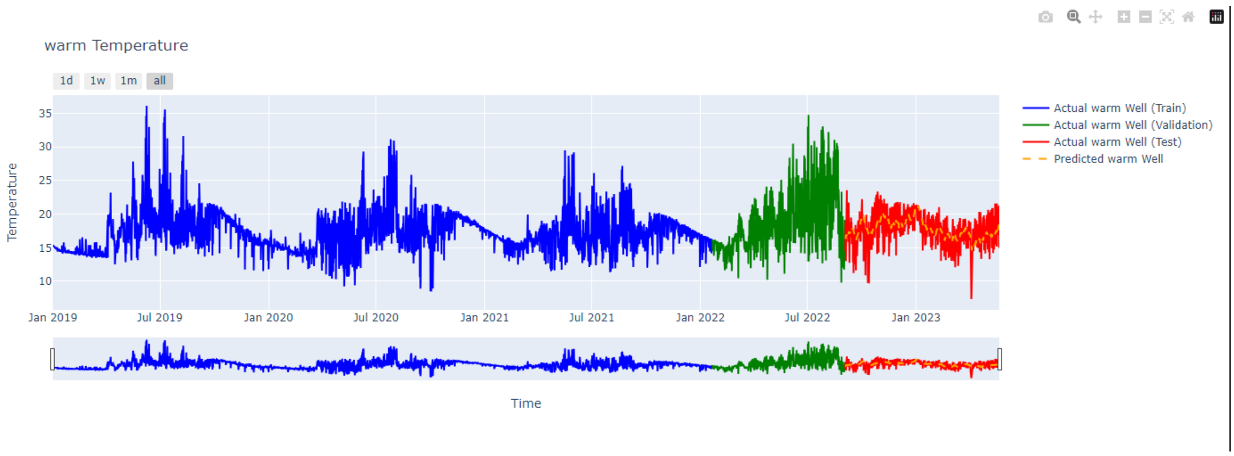

Figure 41: Training, validation, test, and prediction values of warm well temperature

4.2.1.1.3 Singular LSTM model, for predicting one feature (warm well temperature in) at 4 hours data resolution

The results of this experiment, where the model's execution is assessed through the convergence plot, are depicted in Figure 43. The x-axis portrays the epochs of iteration, while the y-axis showcases the evaluation metrics' (loss function) values for the training data. It becomes evident that, after 10 epochs of training, the model begins to stabilize. Furthermore, to guard against overfitting, an early stop function was employed within the LSTM model, causing training to halt after 120 epochs.

In Figure 44, crucial measurements are presented. The Mean Squared Error (MSE) registers at 5.83, the Root Mean Squared Error (RMSE) at 2.41, R-squared (R^2) at 0.23, and the Mean

Absolute Error (MAE) at 1.88. It is noteworthy that R-squared demonstrates a marked improvement compared to previous experiments.

These measurements reveal the model's competence in capturing the overall temperature variation for forecasting purposes, and it outperforms previous experiments. Figure 45 visually underscores this by displaying a comparison between actual temperature values (depicted in blue) spanning nine months and the corresponding predicted values (in orange).

Figure 46 provides a comprehensive overview, encompassing training, validation, test, and predicted values.

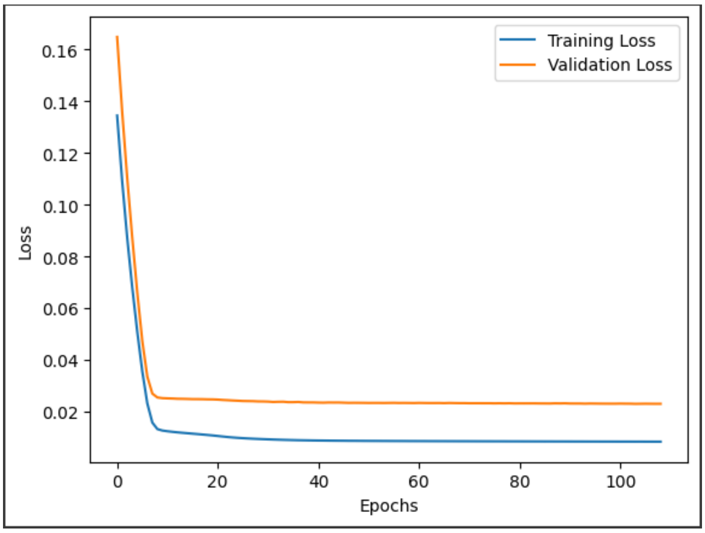

Figure 42: Convergence plot of training and validation losses

```
MSE for Warm Well Temperature: 5.839953537679749

RMSE for Warm Well Temperature: 2.416599581577335

R-squared for warm Well Temperature: 0.23579870173586004
```

```
MAE for warm well: 1.8880717328731556
```

Figure 43: ML model evaluating metrics

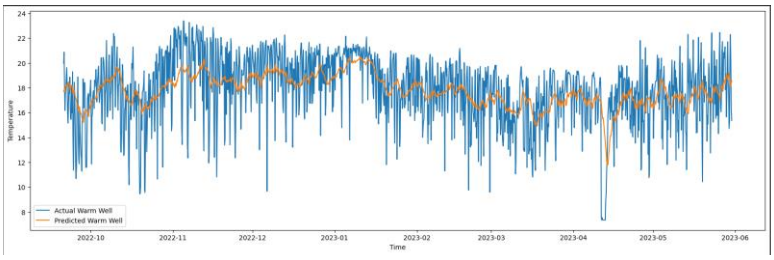

Figure 44: Actual and predicted temperatures for warm well

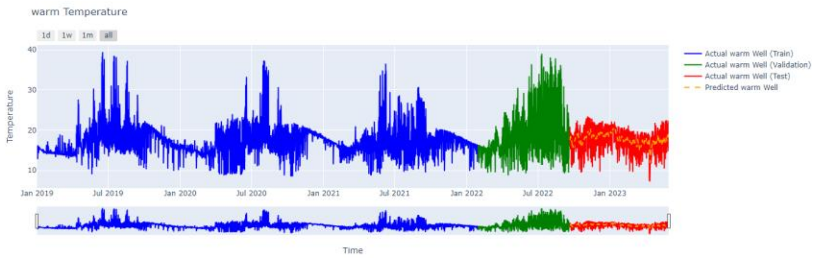

Figure 45: Training, validation, test, and prediction values of warm well temperature

4.2.1.1.4 Summary and key takeaways of the singular LSTM model for predicting one feature

As it is seen increasing the data resolution from 12 hours to 4 hours makes the model to be able to predict the temperature variation trend better.

4.2.1.2 Cascade LSTM model, for predicting one feature (warm well temperature)

This experiment has been designed to compare the results achieved by the singular LSTM model versus the cascade LSTM model. The objective of this experiment was to investigate whether by using a complicated LSTM model is it possible to improve the results for this system. Also decided to change the early stop value to a higher amount to let the model train to higher epochs to evaluate its effect on results.

4.2.1.2.1 Cascade LSTM model, for predicting one feature (warm well temperature) at 1-hour data resolution with 200 epochs

In this experiment, we configured the model to run for a total of 200 epochs, with early stopping criteria set at 5 waiting iterations. Interestingly, the training process halted at the 98th epoch as a preventive measure against overfitting. The convergence plot, presented in Figure 47, reveals that the validation loss stabilized at approximately 0.15, showing no further improvement. However, notable enhancements were observed in the evaluation metrics, with the mean squared error (MSE) registering at 0.0042, the root mean squared error (RMSE) at 0.06, and the coefficient of determination (R^2) at 0.58, as depicted in Figure 48. Furthermore, a visual comparison between actual temperature values and predicted values, as displayed in Figures 49 and 50, underscored some improvements in the model's predictive performance.

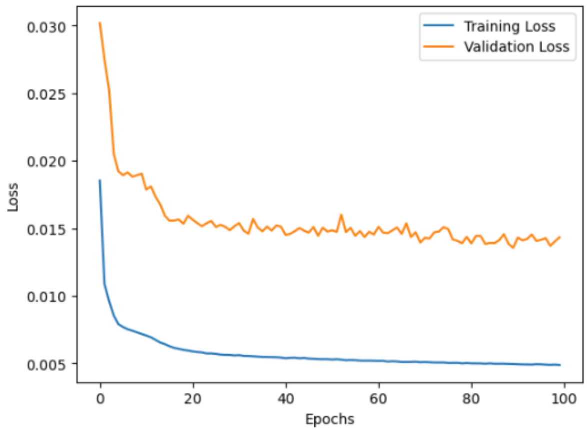

Figure 46: Convergence plot of training and validation losses

```
MSE for Warm Well Temperature: 0.00398127825509882

RMSE for Warm Well Temperature: 0.06309737122177769

R-squared for Warm Well Temperature: 0.6104756159775722
```

Figure 47: ML model evaluating metrics

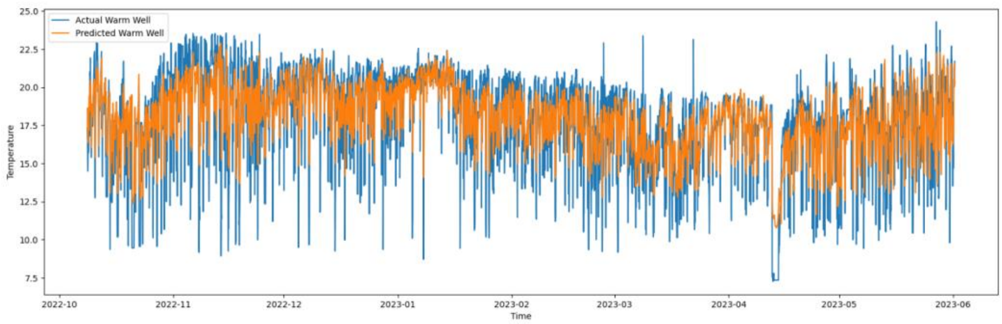

Figure 48: Actual and predicted temperatures for warm well

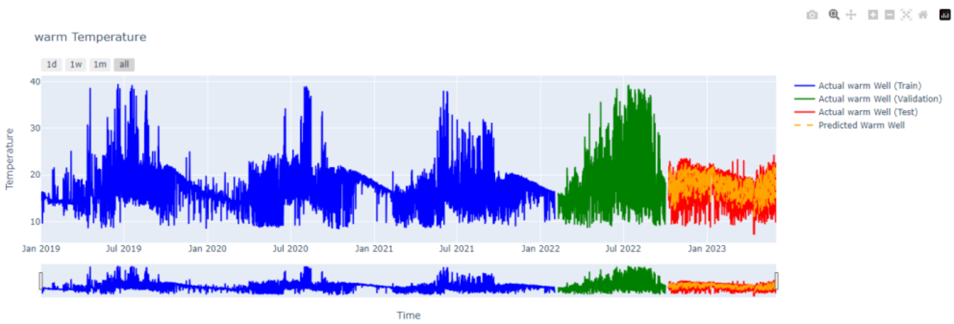

Figure 49: Training, validation, test, and prediction values of warm well temperature

4.2.1.2.2 Cascade LSTM model, for predicting one feature (warm well temperature) at 1-hour data resolution with 2000 epochs

In this experiment, the model was configured to run for a total of 2000 epochs, with early stopping criteria which was set to 55 waiting, the training process was automatically terminated at the 120th epoch as a precautionary measure against overfitting. The convergence plot, as presented in Figure 51, indicated that the validation loss stabilized at approximately 0.18, reflecting a less favorable outcome compared to the previous experiment. Nevertheless, it should be noted that similar results were observed in the evaluation metrics, including a mean squared error (MSE) of 0.0039, a Root mean squared error (RMSE) of 0.062, and a coefficient of determination (R^2) of 0.61, as depicted in Figure 52.

Furthermore, a visual comparison was made between actual temperature values and predicted values, as illustrated in Figures 53 and 54, revealing similar results to the previous experiment.

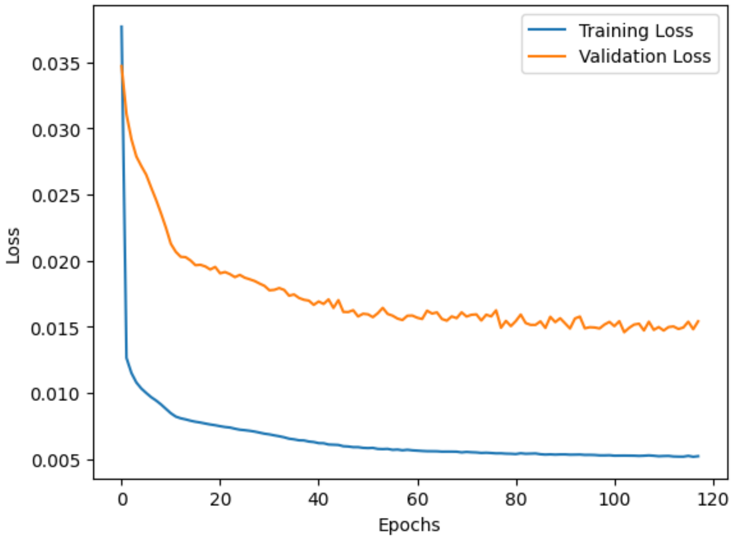

Figure 50: Convergence plot of training and validation losses

```
MSE for Warm Well Temperature: 0.0039657820265354546

RMSE for Warm Well Temperature: 0.06297445534925614

R-squared for Warm Well Temperature: 0.6119917518764095
```

```
MAE for warm well: 0.04634841486058904
```

Figure 51: ML model evaluating metrics

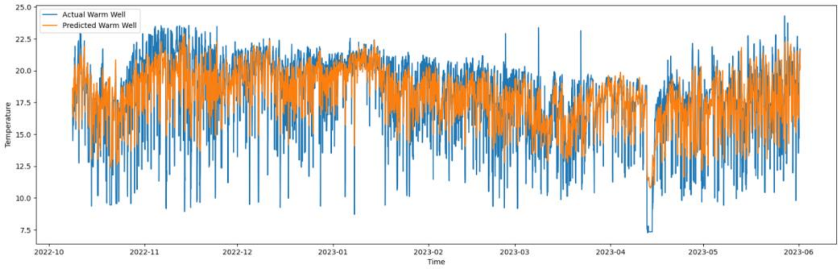

Figure 52: Actual and predicted temperatures for warm well

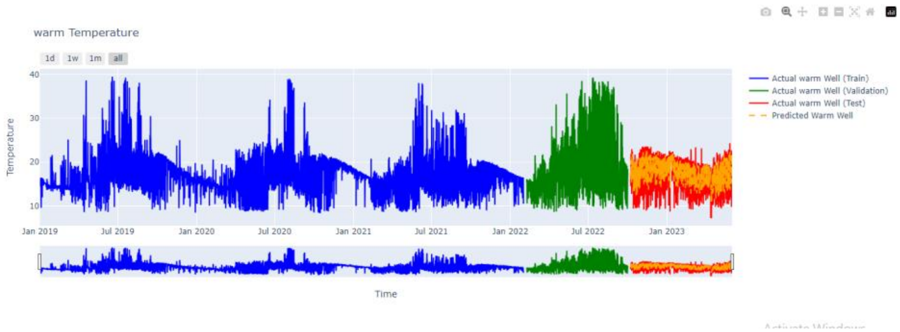

Figure 53: Training, validation, test, and prediction values of warm well temperature

4.2.1.2.3 Summary and key takeaways of the cascade singular LSTM model for predicting one feature

Implementing the cascade LSTM model not only failed to enhance prediction accuracy but also led to a notable increase in training time.

4.2.1.3 Singular LSTM model, for predicting two features (warm well and cold well temperature)

This experiment has been designed to compare the results achieved by the models when one feature (warm well temperature) is predicted versus when two features (warm well temperature and cold well temperature) are predicted by using the singular LSTM. The objective of this experiment is to investigate whether these two features are influenced by each other or not.

4.2.1.3.1 Singular LSTM model, predicting two features (warm well and cold well temperature) - at 5 minutes data resolution

The convergence plot began to stabilize after 13 epochs. There was a noticeable improvement in the loss function, which decreased significantly from 0.03 to 0.001, as shown in Figure 55. Additionally, we observed promising enhancements in the mean squared error (MSE) values for the cold well (0.0005) and warm well (0.0002), root mean squared error (RMSE) for the cold well (0.023) and warm well (0.016), as well as the mean absolute error (MAE) for the cold well (0.012) and warm well (0.0076), as illustrated in Figure 56. Furthermore, a perfect match was evident when comparing the predicted values to the actual values, as demonstrated in Figures 57 and 58.

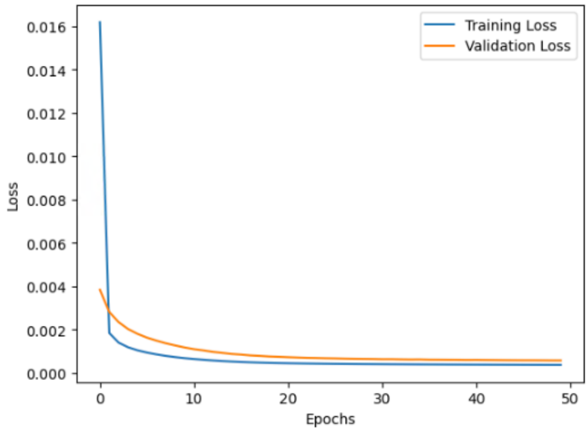

Figure 54: Convergence plot of training and validation losses

```
MSE for Cold Well Temperature: 0.0005586347439271367
MSE for Warm Well Temperature: 0.0002757567213806303

RMSE for Cold Well Temperature: 0.02363545522995351
RMSE for Warm Well Temperature: 0.016605924285646684

R-squared for Cold Well Temperature: 0.8693153612715574
R-squared for Warm Well Temperature: 0.9707322419578277

MAE for cold well: 0.012586704032598539
MAE for warm well: 0.007678661701591531
```

Figure 55: ML model evaluating metrics

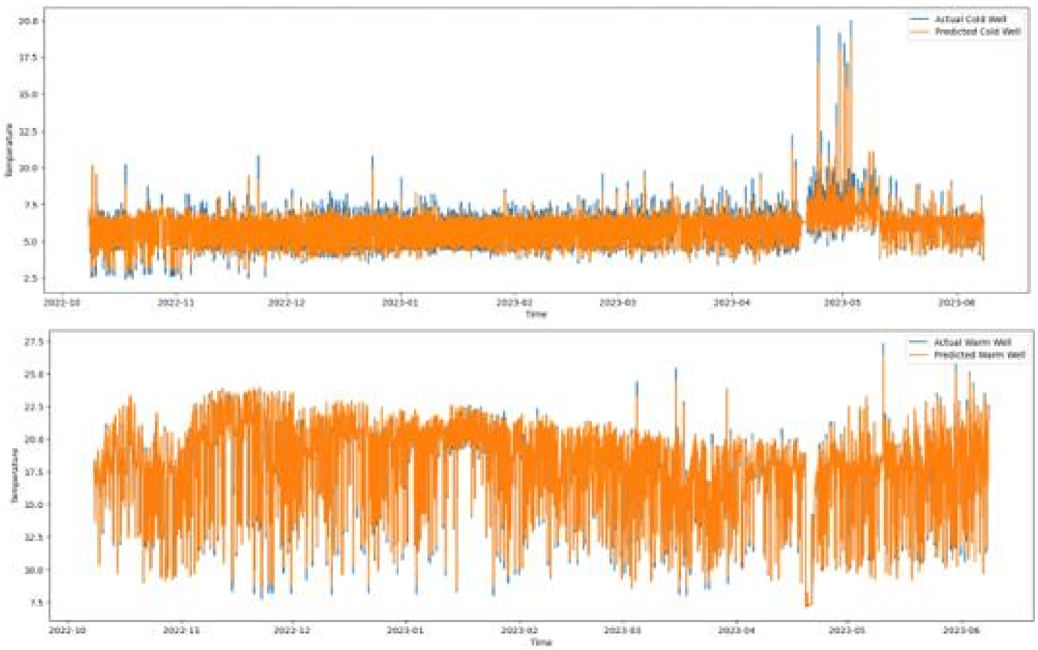

Figure 56: Actual and predicted temperatures for warm well

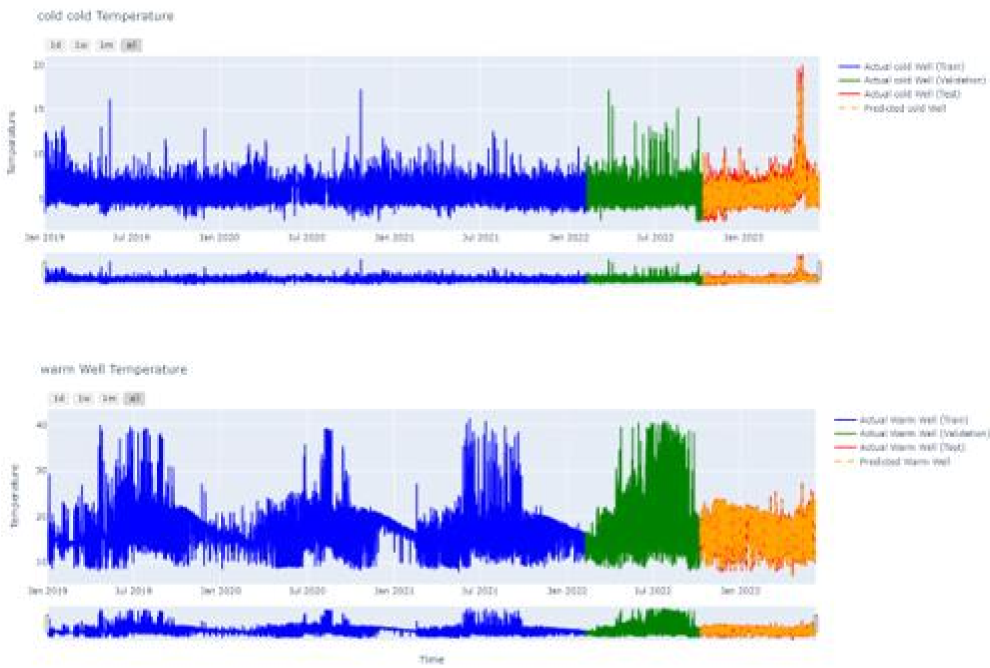

Figure 57: Training, validation, test, and prediction values of warm well temperature

4.2.1.3.2 Summary and key takeaways of the singular LSTM model for predicting two feature

According to the achieved results from the last experiment, it is seen these two features (warm well and cold well temperature) have a direct impact on each other results. Therefore by using higher resolution data (e.g. 5-minute intervals) for predicting two features at the same time, the LSTM model can predict the temperatures precisely.

This approach yielded success with the forecasting horizon of 5 minutes. The upcoming experiments are aimed at extending the forecasting horizon.

4.2.2 Parallel LSTM model

This architecture incorporates two parallel LSTM layers connected to dense layer/layers. LSTM-1 is responsible for sequentially processing historical data spanning the past L days (often referred to as the "look-back window") up until the current time. On the other hand, LSTM-2 handles future time data, utilizing only the forecasted meteorological variable as input at each time step and generating a complete sequence of outputs. It's important to note that for LSTM-2 inputs, only forecasted meteorological variables, specifically environmental temperature, are utilized; no ATES variables such as well temperatures or flow data are included. The outputs from LSTM-1 and LSTM-2 are concatenated and passed to the Dense layer, which generates predictions for the forecast horizon period.

4.2.2.1 Parallel LSTM, 4 inputs to LSTM-2, predicting one feature

4.2.2.1.1 Parallel LSTM, 4 inputs to LSTM-2, predicting one feature, at 12-hour data resolution

Regarding the convergence plot, after just 7 epochs, the early stop mechanism, set to stop after 5 consecutive epochs without improvement, halted the training iterations. The validation loss reached a low of 0.018 remarkably quickly (as shown in Figure 59). Evaluation metrics yielded MSE = 0.005, RMSE = 0.072, R2 = 0.19, and MAE = 0.057, as indicated in Figure 60. Visual comparisons of the predicted values can be observed in Figures 61 and 62.

This LSTM architecture demonstrates an ability to capture temperature patterns to some extent, although the results are not perfect. Previous experiments have shown that higher-resolution data typically enables the LSTM model to better capture system patterns. However, training the model on high-resolution data is time-intensive, taking approximately 7 hours each time of training. This necessitates tuning ML hyperparameters and conducting multiple training runs to optimize the model's performance.

Therefore, the strategy employed was to initially test the model on low-resolution data, adjusting hyperparameters to achieve preliminary results more quickly. In subsequent stages, the data resolution will gradually increase, and new hyperparameter values will be identified and fine-tuned in parallel.

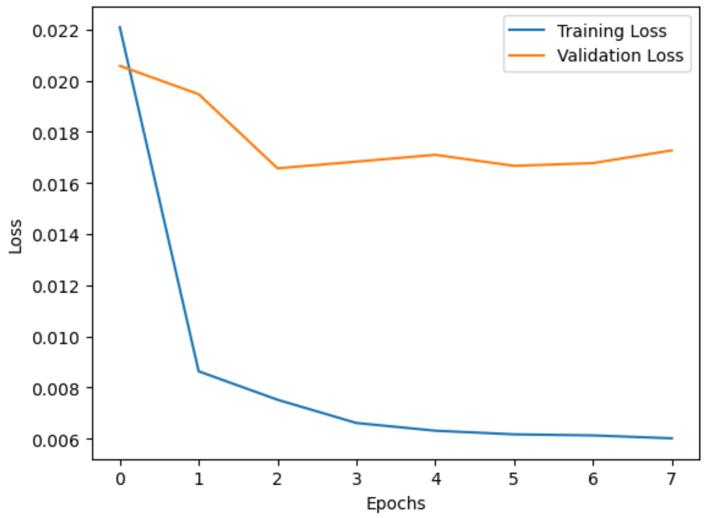

Figure 58: Convergence plot of training and validation losses

```
MSE for Warm Well Temperature: 0.005321973029398249

RMSE for Warm Well Temperature: 0.07295185418752734

R-squared for Warm Well Temperature: 0.19079787334154086

MAE for Warm well: 0.05740063304906067
```

Figure 59: ML model evaluating metrics

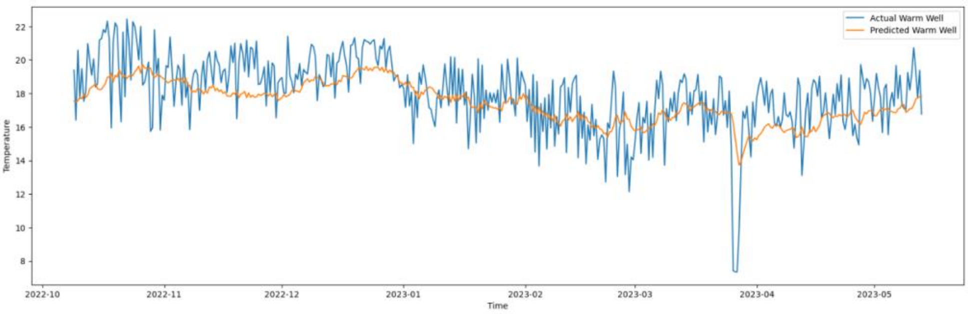

Figure 60: Actual and predicted temperatures for warm well

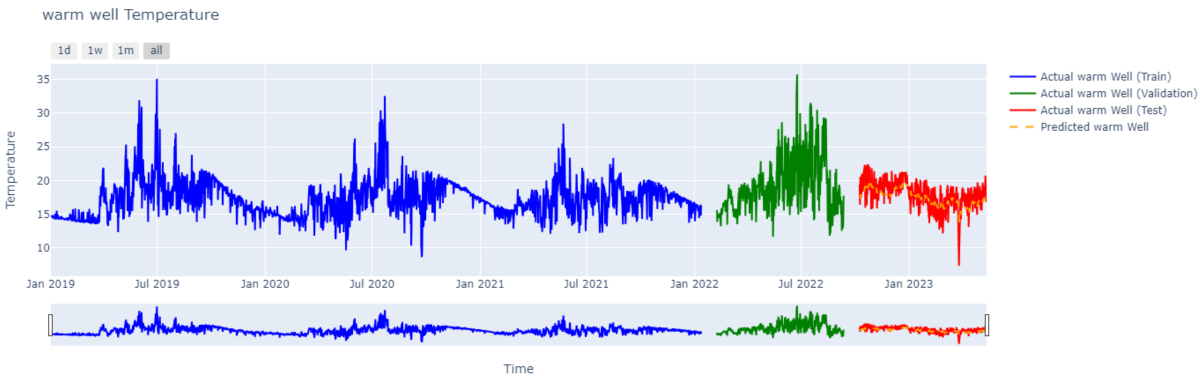

Figure 61: Training, validation, test, and prediction values of warm well temperature

4.2.2.1.2 Parallel LSTM, 4 inputs to LSTM-2, predicting one feature, at 8-hour data resolution

Regarding the convergence plot, the validation loss reached a minimum of 0.014. The early stop mechanism intervened, stopping the training iterations after 68 iterations (as shown in Figure 63). Evaluation metrics, including MSE, RMSE, and MAE, were consistent with previous experiments, while there was a notable improvement in the R^2 value, which reached 0.30, as depicted in Figure 64. Visual comparisons of the predicted values can be observed in Figures 65 and 66. As evident in the graphs below, working with higher-resolution data does increase the time required for model training. However, it results in significantly improved predictions when compared to lower-resolution data.

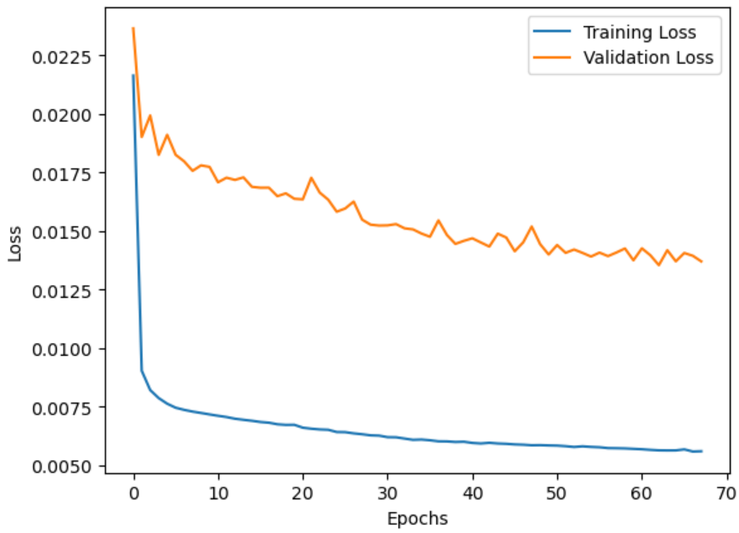

Figure 62: Convergence plot of training and validation losses

```
MSE for Warm Well Temperature: 0.005271365968196637

RMSE for Warm Well Temperature: 0.07260417321474459

R-squared for Warm Well Temperature: 0.3035118982802625

MAE for Warm well: 0.05642594240648399
```

Figure 63: ML model evaluating metrics

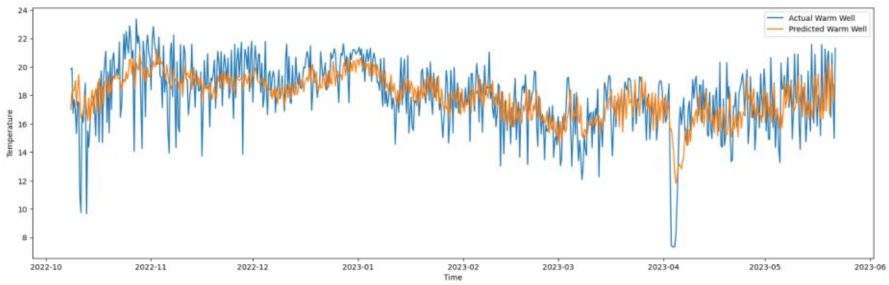

Figure 64: Actual and predicted temperatures for warm well

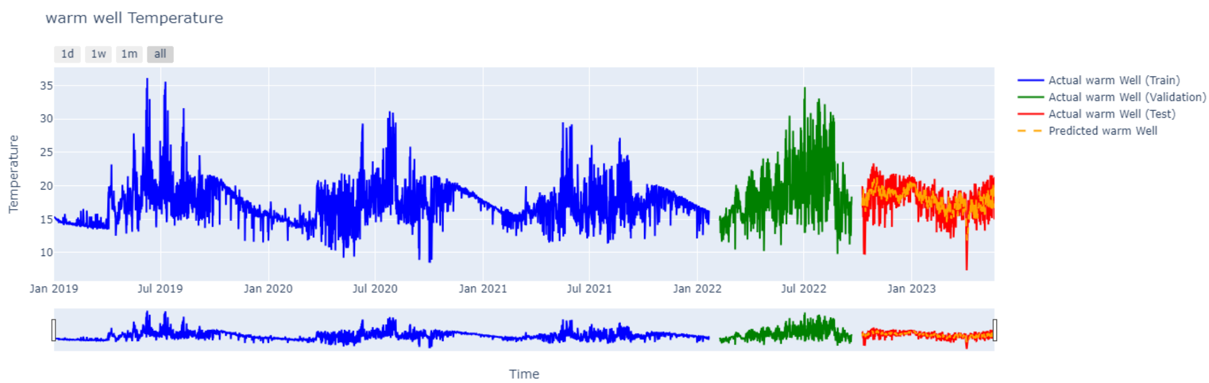

Figure 65: Training, validation, test, and prediction values of warm well temperature

4.2.2.1.3 Parallel LSTM, 4 inputs to LSTM-2, predicting one feature, at 4-hour data resolution

Concerning the convergence plot, the validation loss increased to 0.02 after 99 epochs (as illustrated in Figure 67). The evaluation metrics, including MSE=0.005, RMSE=0.077, and MAE=0.06, showed consistent performance, albeit with a decrease in the R^2 value to 0.25, as indicated in Figure 68. Visual comparisons of the predicted values can be observed in Figures 69 and 70.

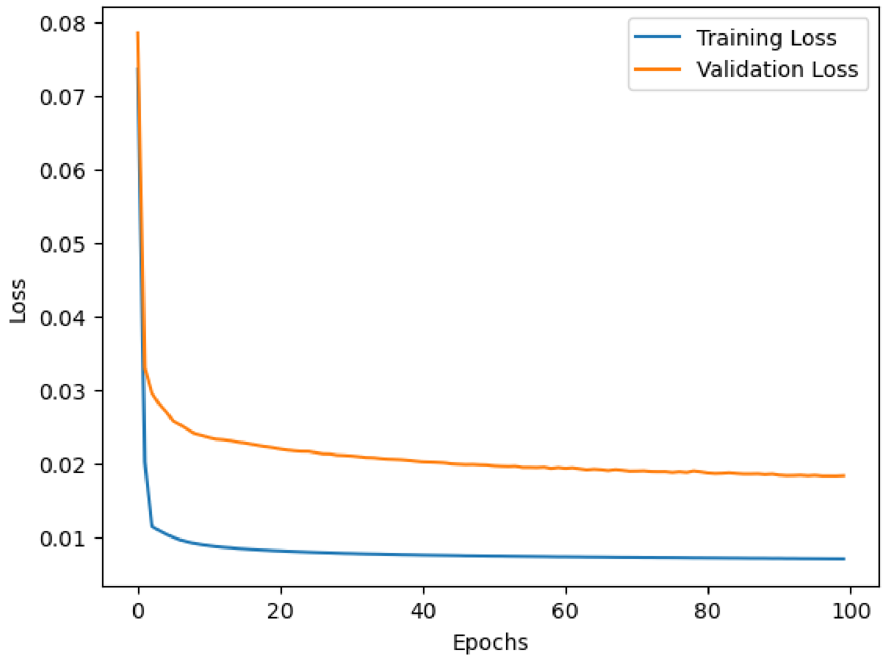

Figure 66: Convergence plot of training and validation losses

```
MSE for warm Well Temperature: 0.005960984308967801

RMSE for warm Well Temperature: 0.07720741097179597

R-squared for warm Well Temperature: 0.25537653691152407

MAE for warm well: 0.060599860271903956
```

Figure 67: ML model evaluating metrics

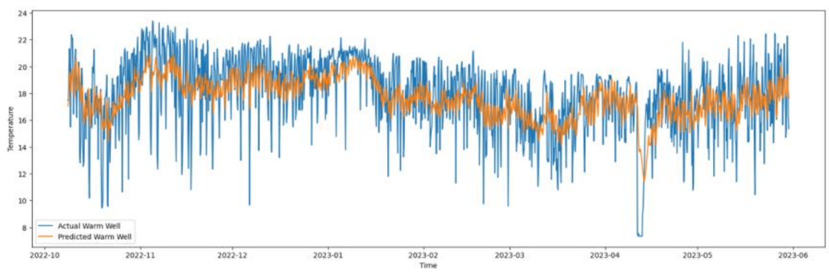

Figure 68: Actual and predicted temperatures for warm well

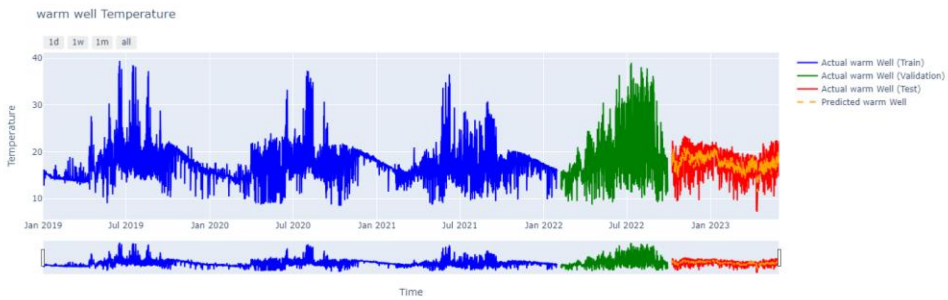

Figure 69: Training, validation, test, and prediction values of warm well temperature

4.2.2.1.4 Parallel LSTM, 4 inputs to LSTM-2, predicting one feature, at 1-hour data resolution

The validation loss stabilized at 0.015 after 86 epochs (as depicted in Figure 71). The evaluation metrics closely resemble those from the previous case, with the notable improvement of the R^2 value, which now stands at 0.41, as shown in Figure 72. Visual comparisons of the predicted values are available in Figures 73 and 74.

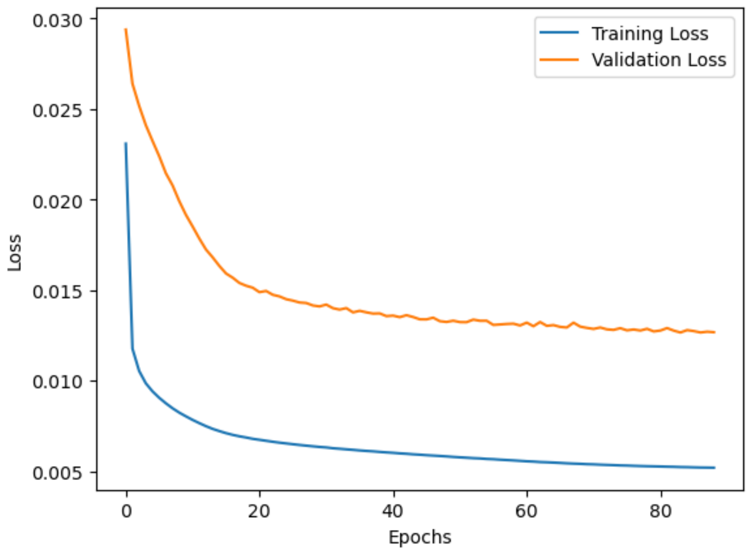

Figure 70: Convergence plot of training and validation losses

```
MSE for warm Well Temperature: 0.005881252804805992

RMSE for warm Well Temperature: 0.0766893265377001

R-squared for warm Well Temperature: 0.4176635466660979

MAE for warm well: 0.05764984975893609
```

Figure 71: ML model evaluating metrics

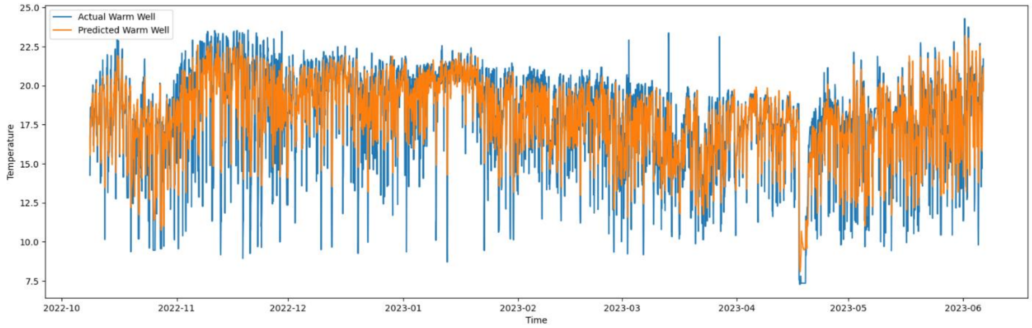

Figure 72: Actual and predicted temperatures for warm well

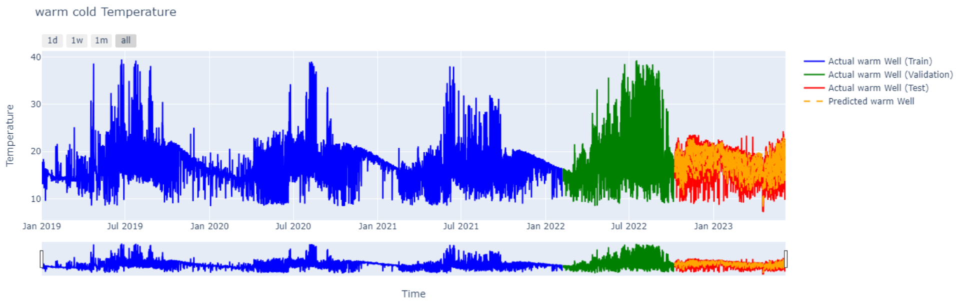

Figure 73: Training, validation, test, and prediction values of warm well temperature

4.2.2.1.5 Parallel LSTM, 4 inputs to LSTM-2, predicting one feature, at 5-min data resolution

A significant improvement was seen in the validation loss stabilized at 0.006 after 38 epochs (as depicted in Figure 75). The evaluation metrics also prove promising results, MSE=0.002, RSME=0.044, R^2 = 0.78. This amount of R square proves that the parallel model can mimic the pattern of time changes acceptably. Predicted values show a notable improvement as shown in Figures 77 and 78.

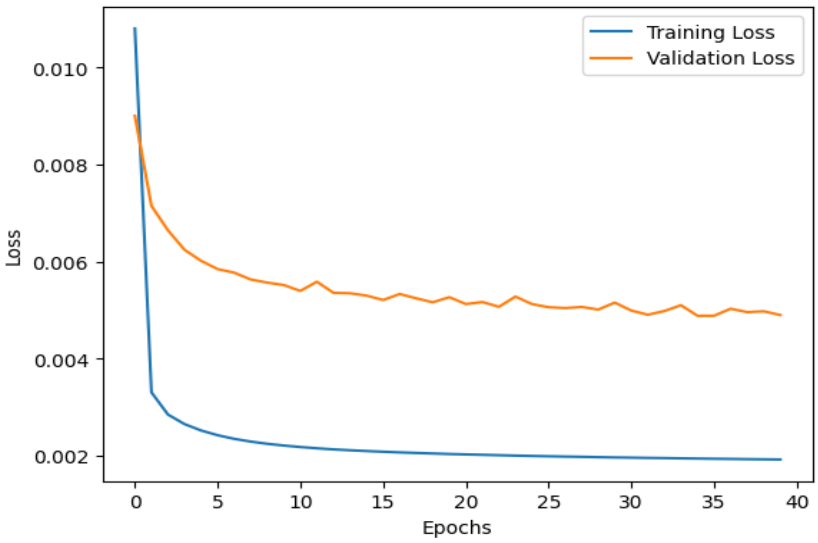

Figure 74: Convergence plot of training and validation losses

```
MSE for warm Well Temperature: 0.002015193505126355

RMSE for warm Well Temperature: 0.044890906708668236

R-squared for warm Well Temperature: 0.786333743546393

MAE for warm well: 0.024943120329797876
```

Figure 75: ML model evaluating metrics

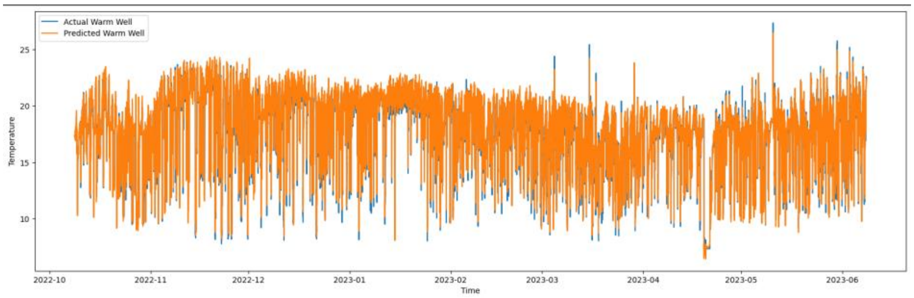

Figure 76: Actual and predicted temperatures for warm well

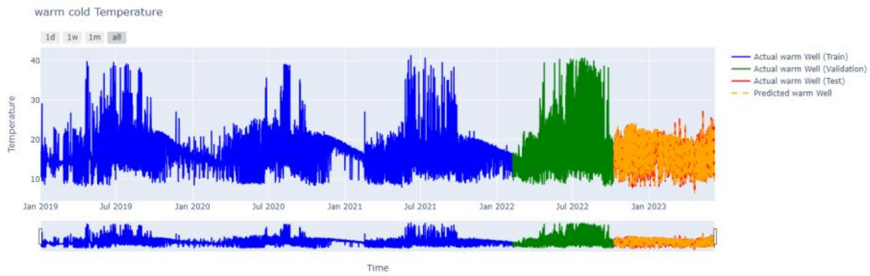

Figure 77: Training, validation, test, and prediction values of warm well temperature

4.2.2.2 Parallel LSTM, 1 input to LSTM-2, predicting two features

4.2.2.2.1 Parallel LSTM, 1 input to LSTM-2, predicting two features by two different dense layers, 4-hour data resolution

Concerning the convergence plot, the validation loss reached its minimum at 0.02. The early stop mechanism triggered, terminating the training iterations after 88 rounds (as displayed in Figure 79). Evaluation metrics for both warm and cold wells are presented in Figure 80. Visual comparisons of the predicted values can be observed in Figures 81 and 82.

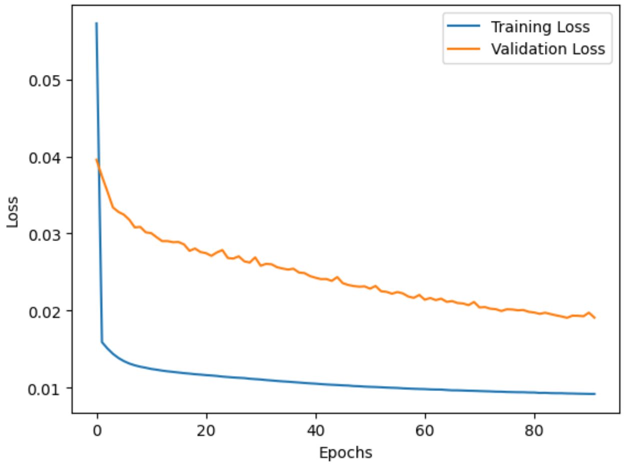

Figure 78: Convergence plot of training and validation losses

```
MSE for Cold Well Temperature: 0.0041138812535690406
MSE for Warm Well Temperature: 0.005291159367602771

RMSE for Cold Well Temperature: 0.06413954516185034
RMSE for Warm Well Temperature: 0.07274035583912668

R-squared for Cold Well Temperature: 0.2742661404899859
R-squared for Warm Well Temperature: 0.3211361680036334

MAE for cold well: 0.04606936100015885
MAE for warm well: 0.057224578801706324
```

Figure 79: ML model evaluating metrics

Figure 80: Actual and predicted temperatures for warm well

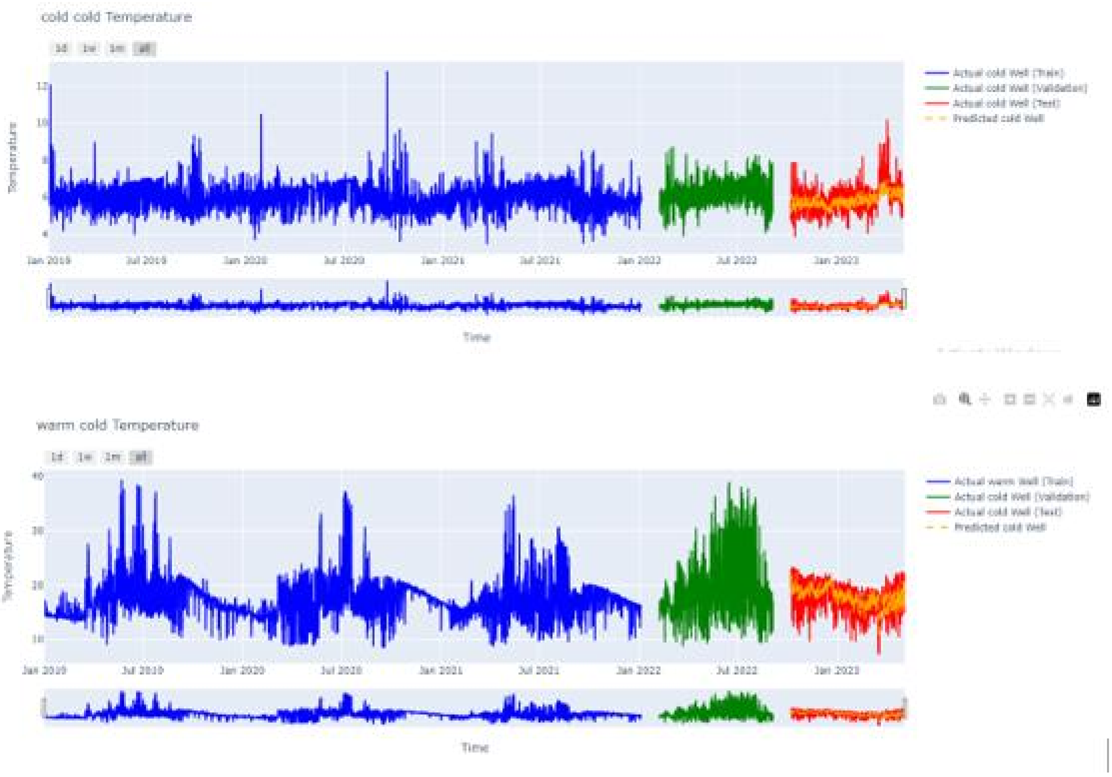

Figure 81: Training, validation, test, and prediction values of warm well temperature

4.2.1.1 Parallel LSTM, 1 input to LSTM-2, predicting two features by two different dense layers, 2-hour data resolution

Concerning the convergence plot, the validation loss reached its minimum at 0.016. The early stop mechanism triggered, terminating the training iterations after 73 rounds (as displayed in Figure 83). Evaluation metrics for both warm and cold wells are presented in Figure 84. Visual comparisons of the predicted values can be observed in Figures 85 and 86.

Comparing the results of the model with one dense layer with a model with two dense layers illustrates the model with one dense layer is able to predict more accurately.

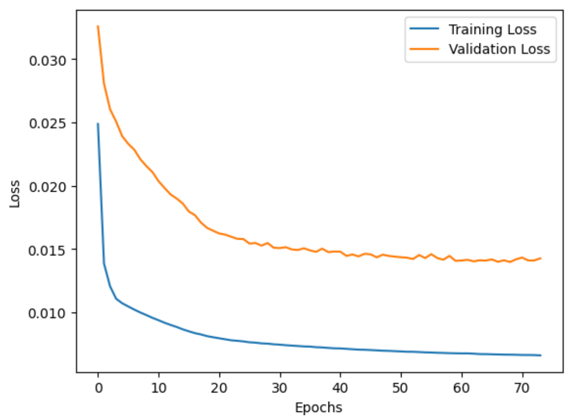

Figure 82: Convergence plot of training and validation losses

```
MSE for Cold Well Temperature: 0.0019506259803255674
MSE for Warm Well Temperature: 0.005290766797985912

RMSE for Cold Well Temperature: 0.04416589159436915
RMSE for Warm Well Temperature: 0.07273765735838564

R-squared for Cold Well Temperature: 0.36491433210469226
R-squared for Warm Well Temperature: 0.43088509294776367

MAE for cold well: 0.032582381642559444
MAE for warm well: 0.0557819882025195
```

Figure 83: ML model evaluating metrics

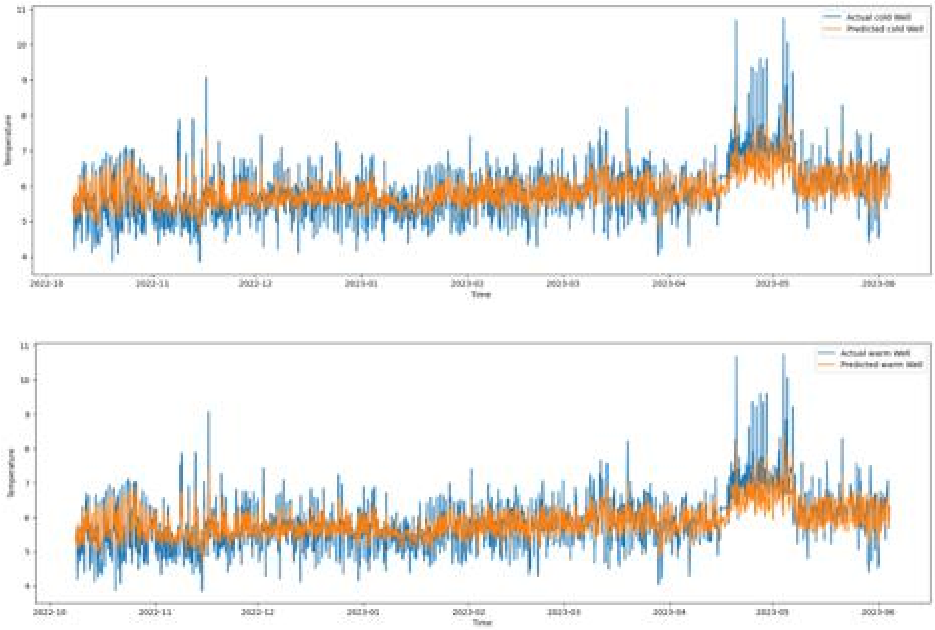

Figure 84: Actual and predicted temperatures for warm well

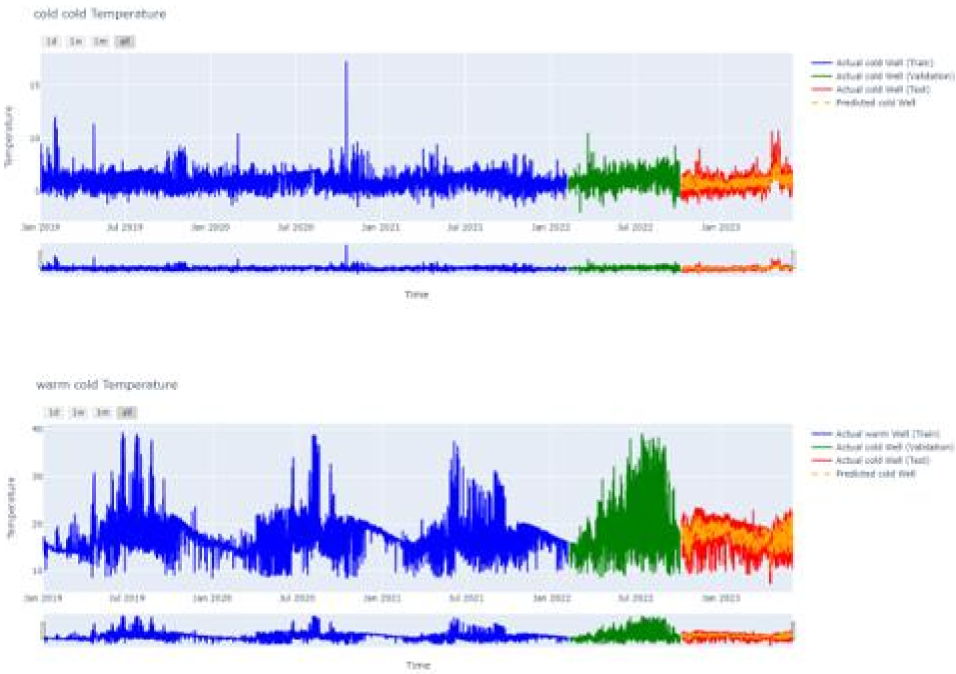

Figure 85: Training, validation, test, and prediction values of warm well temperature

4.2.2.2.2 Parallel LSTM, 1 input to LSTM-2, predicting two features by two different dense layers, 5-min data resolution

The convergence plot illustrates that the validation loss reached its minimum at 0.021. The early stop mechanism triggered, terminating the training iterations after 89 rounds (as displayed in Figure 87). Evaluation metrics for both warm and cold wells are presented in Figure 88. Visual comparisons of the predicted values can be observed in Figures 89 and 90.

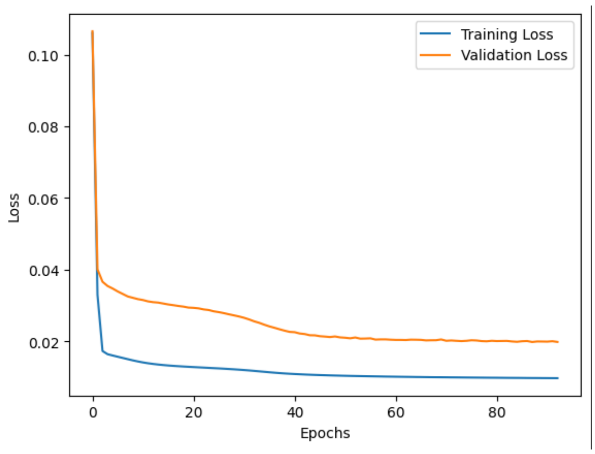

Figure 86: Convergence plot of training and validation losses

```
MSE for Cold Well Temperature: 0.0014924487038666036
MSE for Warm Well Temperature: 0.0011995266612888772

RMSE for Cold Well Temperature: 0.03863222364641471
RMSE for Warm Well Temperature: 0.034634183421713254

R-squared for Cold Well Temperature: 0.6503337407214396
R-squared for Warm Well Temperature: 0.873033433205933

MAE for cold well: 0.024833016056037462
MAE for warm well: 0.022644983878324643
```

Figure 87: ML model evaluating metrics

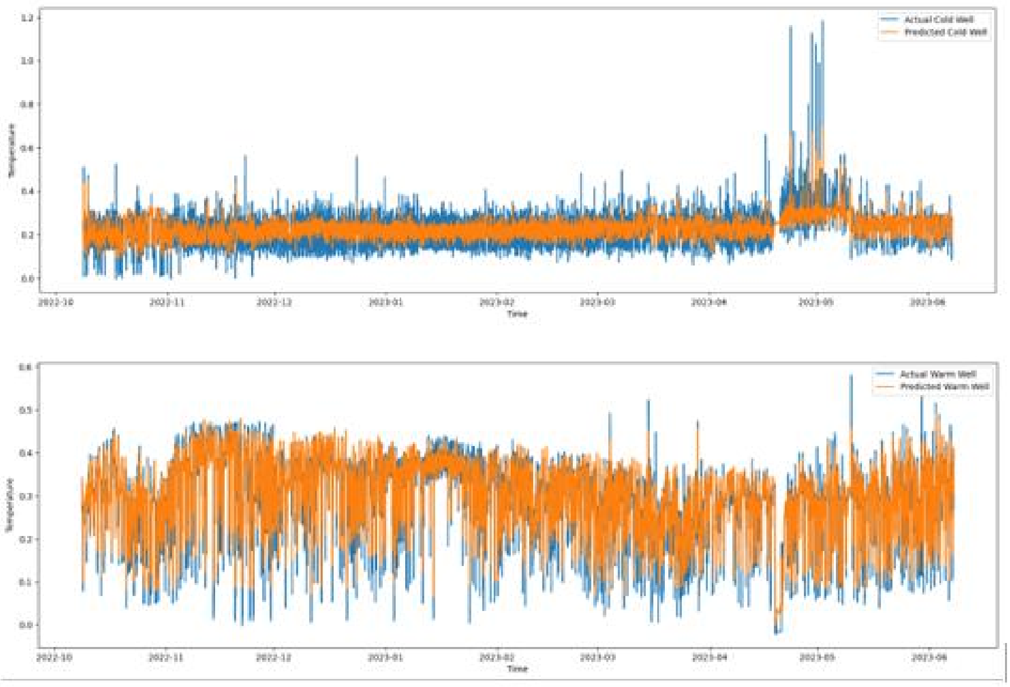

Figure 88: Actual and predicted temperatures for warm well

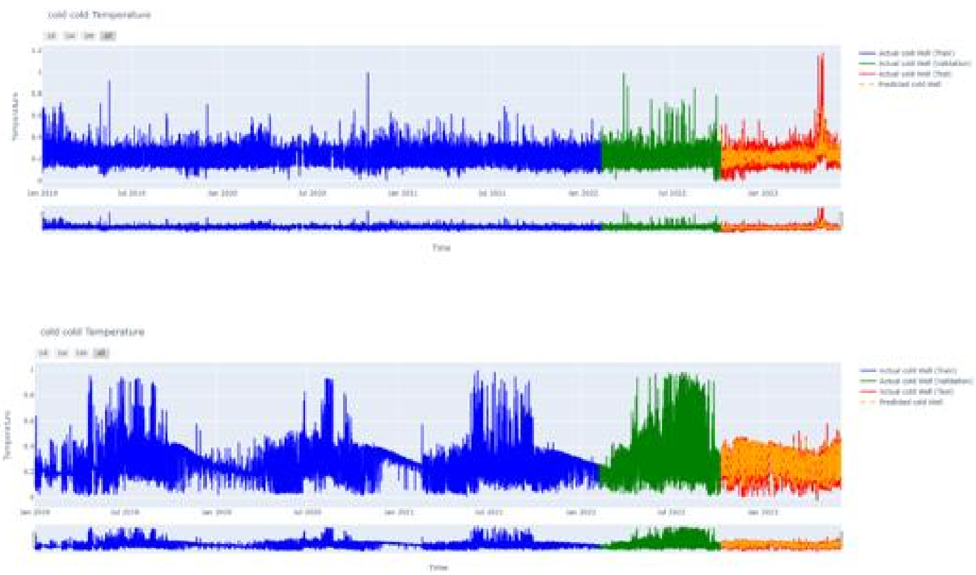

Figure 89: Training, validation, test, and prediction values of warm well temperature

4.3 Discussion

In summary, this study observed temperature variations in the cold and warm wells during heating and cooling cycles. Heating mode accounted for approximately 37.7% of the total operational duration. Temperature fluctuations were most pronounced in water discharged from the heat exchanger, while the charged water into the heat exchanger itself maintained a relatively stable temperature profile.

Analyzing environmental temperature and flow direction revealed clear patterns, with the system switching between heating and cooling modes based on ambient temperature changes. Notably, a strong correlation existed between warm well temperature and environmental temperature, especially when the latter exceeded 15 degrees Celsius, but at times, the warm well temperature surpassed the highest recorded environmental temperature due to additional heat sources.

It is crucial in HE to keep the water temperature above approximately 5 degrees Celsius to prevent freezing in the heat pump evaporator (Bloemendal. M. et. al., 2022), which can create a limitation on the cooler's operating temperature and result in a disconnect between the cold well temperature and the ambient temperature.

To assess the performance of LSTM prediction models, four key evaluation metrics were employed: root mean square error (RMSE), mean absolute error (MAE), mean square error (MSE), and the coefficient of determination (R^2) (Silva. D. G. et. al., 2022).

The root mean squared error (RMSE) is bounded within the range of 0.00 to +inf. The closer its value is to 0.00, the more accurate the predictions are considered, and it aligns with the same scale as the measured data. Equation 3.5 outlines the mathematical formulation of RMSE. Mean absolute error (MAE) calculates the average absolute disparity between predicted and measured values. It can take on values ranging from 0.00 to +inf, with a smaller value indicating more accurate predictions. Importantly, MAE shares the same scale as the measured data. Equation 3.3 illustrates the mathematical representation of MAE. The mean squared error (MSE) quantifies the average squared difference between predicted and measured values, with values in the range of 0.00 to +inf. The closer it is to 0.00, the better. MSE utilizes the same scale as the measured data but squares the differences. Its equation is presented below as (Eq. 3.4). The coefficient of determination (R^2) quantifies a model's predictive effectiveness, ranging from -inf to 1.00. A value closer to 1.00 signifies superior predictive performance. Conversely, a negative R^2 suggests a mismatch between the model's fit and the data trend, a scenario sometimes encountered in non-linear regression models. This coefficient is typically expressed as a percentage and can be defined mathematically, as shown in Equation 3.6.

In conclusion, the effectiveness of LSTM models when applied to ATES time series data has been demonstrated by the attainment of accurate prediction values and favorable evaluation metrics. This study aligns with the recent trend in scientific research, where LSTM models have been the subject of intensive investigation due to their proven ability to effectively model and predict the intricate dynamics of nonlinear and time-varying systems.

Furthermore, a comprehensive exploration of various LSTM cell derivatives and network architectures tailored specifically for time series prediction in the context of ATES data has been provided in this work. This work contributes to the broader body of knowledge, as evidenced by Lindeman's (B.) perspective, by showcasing the valuable role played by LSTM models in advancing our understanding and predictive capabilities within the realm of time series applications. (Lindeman. B. et. al., 2021).

Two different LSTM models were implemented on ATES data. The condensed outcomes, showcasing the R^2, MSE, RMSE, and MAE metrics computed with the optimal hyperparameter settings, have been documented in both Table 1 and Table 2. Moreover, the datasets employed were carefully selected to serve as independent, unseen data, facilitating a robust assessment of the models' performance.

Number of layers	Data resolution	Number of features for prediction	Cold well				Warm well				Forecast horizon
			R^2	RMSE	MSE	MAE	R^2	RMSE	MSE	MAE	
1	12 hr	1	-	-	-	-	0.16	2.025	4.102	1.587	48 hr
1	8 hr	1	-	-	-	-	0.20	2.153	4.638	1.660	32 hr
1	4 hr	1	-	-	-	-	0.23	2.416	5.839	1.888	16 hr
2	1 hr	1	-	-	-	-	0.61	0.063	0.004	-	240 min
1	5 min	2	**0.86**	0.023	0.0005	0.012	**0.97**	0.016	0.000	0.007	5 min

Table 1: Singular LSTM

LSTM-2 inputs	Data resolution	Number of features for prediction	Cold well				Warm well				Forecast horizon
			R2	RMSE	MSE	MAE	R2	RMSE	MSE	MAE	
4	12 hr	1	-	-	-	-	0.19	0.072	0.005	0.057	48 hr
4	8 hr	1	-	-	-	-	0.30	0.072	0.005	0.056	32 hr
4	4 hr	1	-	-	-	-	0.25	0.077	0.005	0.060	16 hr
4	1 hr	1	-	-	-	-	0.41	0.076	0.005	0.057	240 min
4	5 min	1	-	-	-	-	0.78	0.044	0.002	0.024	50 min
1	4 hr	2	0.32	0.072	0.005	0.057	0.27	0.064	0.004	0.046	480 min
1	2 hr	2	0.43	0.072	0.005	0.055	0.36	0.044	0.001	0.032	240 min
1	5 min	2	**0.65**	0.034	0.001	0.022	**0.87**	0.038	0.001	0.024	250 min

Table 2: Parallel LSTM

Overall, both models exhibit reasonably strong performance in predicting well temperatures. The singular model consistently outperforms in terms of accuracy measures such as R^2 and regression errors (MSE, RMSE, and MAE) during training. Conversely, the parallel model excels in predicting over longer periods in each iteration. Both models demonstrate proficiency in predicting unseen data.

For short-term predictions, the singular model offers a quicker response time. However, when it comes to forecasting over longer periods, the parallel model is recommended due to its improved accuracy. It's worth noting that the parallel model, while slower than the singular LSTM model, yields better results with lower loss functions for extended prediction horizons.

Conclusions

Throughout the course of this study, lower temperatures were observed in the cold well during the building heating mode, primarily due to heat being released to the building from water while cold water was stored within the cold well itself. Conversely, higher temperatures were experienced in the warm well during the building cooling mode, as heat was absorbed from the building and warm water was stored within the warm well.

It was noted during this investigation that the heating mode accounted for 37.7% of the total operational duration which is the highest amount in comparison to cooling and shut down mode.

Significantly, the most substantial temperature fluctuations were encountered within the water discharged from the heat, attributable to thermal energy exchange occurring within the heat exchanger (HE). In contrast, a relatively stable temperature profile was maintained by the HE itself, stemming from its source within the well, where temperatures remained relatively constant over time.

When temperature variations between the environment and flow direction were compared, distinct patterns were unveiled. Typically, the system operated in heating mode when the external temperature fell below 10 degrees Celsius, transitioning into cooling mode as the ambient temperature progressively increased. Subsequently, the heating mode was resumed as temperatures decreased once more.

Furthermore, an intriguing correlation was observed when temperature variations between the environment and well temperatures were analyzed. A robust association was identified between warm well temperature and environmental temperature, particularly when the latter exceeded 15 degrees Celsius. Under such conditions, these two variables were found to closely align. However, it is worth noting that on occasion, the highest recorded environmental temperature was surpassed by the warm well temperature. This phenomenon could be attributed to supplementary heat sources, such as solar panels and waste heat from neighboring companies, injecting additional energy into the water, thereby elevating the warm well temperature.

It is of paramount importance to ensure that the water temperature remains above a specific threshold, typically set around 5 degrees Celsius, to prevent the risk of freezing within the heat pump condenser. This precautionary measure, aimed at avoiding freezing within the heat pump system, especially during extremely low temperatures, results in a constraint being imposed on the cooler's operating temperature. Consequently, this limitation may lead to a disparity between the cold well temperature and the prevailing ambient temperature.

In the context of LSTM models used for temperature forecasting, it's important to note that both singular and parallel LSTM models excel at predicting future temperatures with high precision. However, they differ in terms of training time and forecasting capabilities.

The singular LSTM model requires a longer training period to achieve high prediction accuracy, but it specializes in forecasting within a relatively short time window, typically up to 5 minutes into the future. In contrast, the parallel LSTM model, while having a shorter training time, can provide forecasts that extend approximately 50 times further into the future compared to the singular model. This means the parallel LSTM model offers both faster training and the ability to make predictions over much longer time periods.

To sum up, the parallel LSTM model not only trains more quickly but also extends its forecasting horizon significantly beyond that of the singular LSTM model. This performance difference highlights the value of the parallel LSTM approach, particularly in applications where rapid training and extended forecasting are important considerations.

References

Bloemendal, M., Beernink, S., Bel, N. v., Hockin, A., & Schout, G. (2020). Transitie open bodemenergiesysteem Koppert-Cress naar verhoogde opslagtemperatuur. Retrieved from Nieuwegein

www.knmi.nl (online) (09 June 2023 – 06 August 2023)

Jonte Dancker. (2022). A Brief Introduction to Recurrent Neural Networks. https://towardsdatascience.com/a-brief-introduction-to-recurrent-neural-networks-638f64a61ff4

Gauch, M., Kratzert, F., Klotz, D., Nearing, G., Lin, J., & Hochreiter, S. (2021). Rainfall–runoff prediction at multiple timescales with a single Long Short-Term Memory network. Hydrology and Earth System Sciences, 25(4), 2045–2062. https://doi.org/10.5194/hess- 25-2045-2021

Kratzert, F., Klotz, D., Brenner, C., Schulz, K., & Herrnegger, M. (2018). Rainfall–runoff modelling using Long Short-Term Memory (LSTM) networks. Hydrology and Earth System Sciences, 22(11), 6005–6022. https://doi.org/10.5194/hess-22-6005-2018

Kratzert, F., Klotz, D., Shalev, G., Klambauer, G., Hochreiter, S., & Nearing, G. (2019). Towards learning universal, regional, and local hydrological behaviors via machine learning applied to large-sample datasets. Hydrology and Earth System Sciences, 23(12), 5089– 5110. https://doi.org/10.5194/hess-23-5089-2019

Beernink Stijn, Bloemendal Martin, Kleinlugtenbelt Rob, Hartog Niels. (2022). Maximizing the use of aquifer thermal energy storage systems in urban areas: effects on individual system primary energy use and overall GHG emissions. Applied Energy. 311, 118587. https://www.sciencedirect.com/science/article/pii/S030626192200068X

Casasso Alessandro, Giordano Nicolò, Bianco Carlo, and Sethi Rajandrea. (2022). UTES - Underground Thermal Energy Storage. Encyclopedia of Energy Storage. (1), 382-393. https://doi.org/10.1016/B978-0-12-819723-3.00078-0

Martin Bloemendal, Stijn Beernink, Niels Hartog. (2022). Transition of ATES to HT-ATES: Field monitoring results of thermal impact and well temperature. European Geothermal Congress.

Bouchefry Khadija El, Souza Rafael S. de. (2020). Knowledge Discovery in Big Data from Astronomy and Earth Observation. 225-249. https://www.sciencedirect.com/science/article/pii/B9780128191545000230

Shamshirband, S., Hashemi, S., Salimi, H., Samadianfard, S., Asadi, E., Shadkani, S., Kargar, K., Mosavi, A., Nabipour, N., & Chau, K.-W. (2020). Predicting Standardized Streamflow index for hydrological drought using machine learning models. Engineering Applications of Computational Fluid Mechanics, 14(1), 339–350. https://doi.org/10.1080/19942060.2020.1715844

Wencheng Jin, Trevor A. Atkinson, Christine Doughty, Ghanashyam Neupane, Nicolas Spycher, Travis L. McLing, Patrick F. Dobson, Robert Smith, Robert Podgorney. (2022).

Machine-learning-assisted high-temperature reservoir thermal energy storage optimization. Renewable Energy, 384-397.
https://www.sciencedirect.com/science/article/pii/S0960148122011405

X. Shi, S. Jiang, H. Xu, F. Jiang, Z. He, J. Wu. (2016). The effects of artificial recharge of groundwater on controlling land subsidence and its influence on groundwater quality and aquifer energy storage in Shanghai, China, Environ. Earth Sci. 75 (3) (2016) 195. http://dx.doi.org/10.1007/s12665-015-5019-x.

W. Jin, R. Podgorney, T. McLing, R. Carlsen. (2021). Geothermal battery optimization using stochastic hydro-thermal simulations and machine learning algorithms, in: 55th US Rock Mechanics/Geomechanics Symposium, OnePetro.

K.J. Bergen, P.A. Johnson, V. Maarten, G.C. Beroza. (2019). Machine learning for data driven discovery in solid earth geoscience, Science 363 (6433).
http://dx.doi.org/10.1126/science.aau0323.

Silva Davi Guimarães da, Geller Marla Teresinha Barbosa, Moura Mauro Sérgio dos Santos, Meneses Anderson Alvarenga de Moura. (2022). Performance evaluation of LSTM neural networks for consumption prediction. e-Prime - Advances in Electrical Engineering, Electronics and Energy.
https://www.sciencedirect.com/science/article/pii/S2772671122000031

Lindema nn Benjamin, Müller Timo, Vietz Hannes, Jazdi Nasser, Weyrich Michael. (2021). A survey on long short-term memory networks for time series prediction. 14th CIRP Conference on Intelligent Computation in Manufacturing Engineering, CIRP ICME '20.